



ALICE-ANA-2014-xxx
April 6, 2018

Production of ${}^3_{\Lambda}\text{H}$ and ${}^3_{\Lambda}\bar{\text{H}}$ in Pb–Pb collisions at $\sqrt{s_{\text{NN}}}=5.02$ TeV

Stefano Trogolo^{1,2}, Stefania Bufalino^{2,3}, Elena Botta^{1,2}

1. Università degli Studi di Torino

2. INFN - Torino

3. Politecnico di Torino

Email: strogolo@cern.ch

Abstract

In this analysis note the details and results of the measurement of the ${}^3_{\Lambda}\text{H}$ and ${}^3_{\Lambda}\bar{\text{H}}$ production in Pb–Pb collisions at $\sqrt{s_{\text{NN}}}=5.02$ TeV are presented. The goals of this analysis are the hypertriton transverse momentum spectra $d^2N/(dydp_t)$ have been studied together with the dN/dy evolution with the particle multiplicity of the collision to have a comparison with the prediction of the models that are typically used to describe the particle production in heavy ion collision, namely statistical-thermal and coalescence models.

In particular the $dN/dy \times \text{B.R.}$ measured in 0–10%, 10–30% and 30–50% for the ${}^3_{\Lambda}\text{H}$ and the ${}^3_{\Lambda}\bar{\text{H}}$ will be presented. Moreover, it has been possible to calculate the antimatter-to-matter ratio, the ${}^3_{\Lambda}\text{H}/{}^3\text{He}$ ratio and the S_3 (${}^3_{\Lambda}\text{H}/{}^3\text{He} \times p/\Lambda$). Finally, the p_{T} -spectra has been measured in the 10–40% centrality class and the coalescence parameter B_3 has been evaluated as well.

18 **Contents**

19	1 Introduction	2
20	2 Data sample	2
21	2.1 Data	2
22	2.2 Monte Carlo	3
23	3 Event selection	4
24	3.1 Selected data sample	5
25	4 Hypertriton reconstruction	7
26	4.1 (Anti-) $^3_{\Lambda}\text{H}$ candidates selection and PID	8
27	4.2 Decay vertex selection	10
28	5 Production yields vs centrality	13
29	5.1 Raw yields extraction vs centrality	13
30	5.2 Efficiency correction	17
31	5.3 Absorption correction	19
32	5.4 Systematics uncertainties	21
33	5.5 Corrected yields	25
34	6 p_{T} production spectra	26
35	6.1 Raw yields extraction vs p_{T}	26
36	6.2 Efficiency correction	30
37	6.3 Absorption correction	30
38	6.4 Systematics uncertainties	31
39	7 Results	34
40	7.1 p_{T} spectra	34
41	7.2 dN/dy as a function of centrality	36
42	7.3 Antimatter-to-matter ratio	38
43	7.4 $^3_{\Lambda}\text{H}$ over ^3He ratio	39
44	7.5 S_3 ratio	40
45	7.6 Comparison with thermal model	42
46	7.7 Coalescence parameter	43
47	7.8 Thermal fit	46

1 Introduction

The hypertriton (${}^3_{\Lambda}\text{H}$) is the lightest known hypernucleus and is formed by a proton, a neutron and a Λ baryon. ${}^3_{\Lambda}\text{H}$ mesonic charged decay channels are:

$${}^3_{\Lambda}\text{H} \rightarrow {}^3\text{He} + \pi^- \quad (1)$$

$${}^3_{\Lambda}\text{H} \rightarrow \text{d} + \text{p} + \pi^- \quad (2)$$

$${}^3_{\Lambda}\text{H} \rightarrow \text{p} + \text{n} + \text{p} + \pi^- \quad (3)$$

and their charge conjugate.

The most recent evaluation of the B.R. of the ${}^3_{\Lambda}\text{H}$ weak decay channels is presented in [1]. The results therein led to a B.R. for the two body mesonic weak decay channel (1) of 37%, considering both the charged and neutral modes, while the charged decay channel has a B.R. of 25%. This latter value will be used in all the analysis note.

In this analysis note, we present the details of the analysis technique used to extract the production yields and p_{T} -spectra of ${}^3_{\Lambda}\text{H}$ and ${}^3_{\Lambda}\bar{\text{H}}$ in the 2 body decay channel (1) in Pb–Pb collisions at $\sqrt{s_{\text{NN}}} = 5.02$ TeV.

2 Data sample

2.1 Data

The analysis presented in this note is based on the data set of Pb–Pb collisions at $\sqrt{s_{\text{NN}}} = 5.02$ TeV collected in 2015. The collisions in the LHC were delivered at different interaction rates: the low interaction rate (300-400 Hz) and the high interaction rate (1-7.5 kHz). The events were acquired when a coincidence of signals for both sides of the V0 detector was found, the so called *Minimum Bias* trigger (MB). Moreover, the time information of the V0 scintillator arrays paired with the same information of the ZDC is used to reject offline events triggered by the interaction of the beams with the residual gas in the LHC vacuum pipe. Since many analyses in the ALICE experiment require a large amount of statistics, also events with an incomplete TPC acceptance were collected and are used in this analysis. The sample of collected data consists of nearly 154×10^6 minimum bias events. The *LHC15o* runlists used are the following:

LHC15o_highIR_pass1

- *DPG_CentralBarrelTracking_20161130_v6*: 246994, 246991, 246989, 246984, 246982, 246980, 246948, 246945, 246928, 246851, 246847, 246846, 246845, 246844, 246810, 246809, 246808, 246807, 246805, 246804, 246766, 246765, 246763, 246760, 246759, 246758, 246757, 246751, 246750, 246495, 246493, 246488, 246487, 246434, 246431, 246428, 246424, 246276, 246275, 246272, 246271, 246225, 246222, 246217, 246185, 246182, 246181, 246180, 246178, 246153, 246152, 246151, 246148, 246115, 246113, 246089, 246087, 246053, 246052, 246049, 246048, 246042, 246037, 246036, 246012, 246003, 246001, 245963, 245954, 245952, 245949, 245923, 245833, 245831, 245829, 245705, 245702, 245700, 245692, 245683

- *DPG_CentralBarrelTracking_TPCreduced_20161221_v6*: 246871, 246870, 246867, 246865, 246676, 246675

LHC15o_highIR_pass1_pidfix

- *DPG_CentralBarrelTracking_20161018_v0*: 245232, 245231, 245152, 245151, 245146, 245145

83 - *DPG_CentralBarrelTracking_TPCreduced_20161221_v0*: 245554, 245545, 245544, 245543, 245542,
84 245540, 245535, 245507, 245505, 245504, 245501, 245497, 245496, 245454, 245452, 245450,
85 245446, 245441, 245439, 245411, 245409, 245407, 245401, 245397, 245396, 245353, 245349,
86 245347, 245346, 245345, 245343, 245259

87 **LHC15o_lowIR_pass3_pidfix**

88 - *DPG_CentralBarrelTracking_20161109_v0*: 244918, 244975, 244980, 244982, 244983, 245064,
89 245066, 245068, 246390, 246391, 246392

90 2.2 Monte Carlo

91 The Monte Carlo (MC) sample, used to study the cuts applied in the analysis and to compute the effi-
92 ciency and acceptance corrections, was generated using the HIJING event generator [2]. The data taking
93 conditions are accounted in the MC by reproducing the configuration of the different detectors in the
94 runs used for the analysis. Since the HIJING event generator used to simulate a Pb–Pb collision does not
95 include any (anti-)(hyper-)nucleus, an *ad-hoc* generator was used to inject them on top of each HIJING
96 event. The kinematics of the injected hypernuclei is chosen randomly, since their production spectra in
97 heavy ion collisions are barely or completely unknown. The transverse momentum p_T is picked from
98 a flat distribution in the range between 0 and 10 GeV/c, the azimuthal angle ϕ from a flat distribution
99 between 0 and 2π radians and the rapidity from a flat distribution in the range $|y| < 1$.

Monte Carlo productions				
Label	Anchor period	b (fm)	Injected particles per event (+ charge conjugate)	Events
LHC16h7a	Pb–Pb $\sqrt{s_{NN}}=5.02$ TeV	0-5	10x (H^2, H^3, He^3, He^4); 40x $\frac{3}{\Lambda}H$; 20x ($\frac{4}{\Lambda}H, \frac{3}{\Lambda}He$)	112112
LHC16h7b		5-11		439760
LHC16h7c		11-15		355740
LHC17d5a	Pb–Pb	11-15	injection as LHC16h7, +4.5% material budget	444,300
LHC17d5b	$\sqrt{s_{NN}}=5.02$ TeV	11-15	injection as LHC16h7, -4.5% material budget	444,240

Table 1: Details about the MC productions used in this analysis. The particles are injected on top of each HIJING event and the injection scheme is the same for all the productions. The number of injected particles has to be multiplied by 2 to count also the respective charge conjugate states. The impact parameter (b) is extracted from a flat distribution with the limits reported in the table.

100 The MC simulation of a full Pb–Pb event, from the generation of the kinematics of the particles up to
101 the final event reconstruction, is extremely expensive in terms of computing resources (\sim one hour for
102 one central Pb–Pb event on the ALICE Grid). Thus, only a fraction of the total collected statistics is
103 simulated and reconstructed in the MC samples. The centrality of the simulated event is determined by
104 the impact parameter (b), which is extracted randomly from a flat distribution. The b_{min} and b_{max} of the
105 distribution have been chosen to match the edges of the centrality distribution of the real data. In order to
106 optimise the computing resources usage, the MC production anchored to the 2015 Pb–Pb data is divided
107 in three different sub-samples corresponding to three different b intervals. These three MC productions
108 corresponds to the 0-10%, 10-50% and 50-90% VOM centrality intervals. The anchor period and the b
109 intervals used in each sub-sample as well as the number of injected particles in each HIJING event are
110 reported in Table 1.

111 Two additional MC samples have been produced to evaluate the systematics effect of the uncertainty on
112 the material budget determination in ALICE. The material budget is increased and decreased of 4.5%
113 with respect to the nominal amount in the MC samples, as reported in Table 1. These variations have
114 been driven by the results obtained from the photon conversion analyses performed in ALICE[3]. Since

the uncertainty on the material budget determination is independent from the collision centrality, only the most peripheral collisions ($b \rightarrow 11-15$ fm), which require less computing resources, have been simulated. These MC production was done using the *AliDPG* [4] package, where all the configurations have been set in the PWGLF custom generators `Hijing_Nucleon004.C`

3 Event selection

The collected events are further selected offline to reduce possible biases from particular data taking conditions. All the events are required to be minimum bias trigger, as already mentioned. Events with the primary vertex outside the fiducial region of ± 10 cm in the beam direction from the nominal interaction point are rejected ($|V_z| \leq 10$ cm). These selections are the standard ones used in the analysis of Pb–Pb events, which guarantee a symmetric acceptance and the rejection of beam-gas events.

An important consequence of the high interaction rate in 2015 data taking, is the presence of *pile-up* in triggered events. These events contain more than one primary collision vertex. The first selection applied to remove the pile-up is on the number of primary vertices reconstructed with SPD with more than n contributors. The number of contributors is the number of SPD tracklets used to estimate the vertex position. The choice of the n parameter depends on the multiplicity of the events and it is driven by the multiplicity dependence of false positive pile-up tagging of previous analyses. It is set to 3 for events with less than 20 tracklets, to 5 for events with more than 50 tracklets and to 4 for the remaining events. This selection based on the SPD vertex finding can remove the pile-up of collisions occurring either in the same bunch crossing¹ or out of bunch within the SPD readout time (300 ns). Nevertheless, the aforementioned criterion is not able to resolve and remove collisions spaced by less than 8 mm along the beam axis. These pile-up collisions are merged and treated as a single one.

The second selection criterion used to reduce the pile-up background is based on the correlation between different centrality estimators. The correlation, reported in Figure 1a, between the centrality estimator V0M, based on the V0 detectors, and CL0, based on the SPD clusters, shows some outliers which are interpreted as events with residual pile-up. The correlation has been parametrized and the obtained correlation function allows to compute the expected V0M percentile corresponding to a given value of CL0. Consequently, the outliers can be removed with a 5σ selection on the aforementioned correlation, where σ is the resolution of the correlation distribution. Figure 1a and Figure 1b show the correlation between the V0M and CL0 centrality estimators before and after the event selection. It is possible to see how the selection cleans the correlation plot, removing the outliers. Another possibility is to remove the outliers in the correlation, shown in Figure 1c, between the V0M centrality estimator and the number of SPD tracklets. In this case, it is possible to see how the selection on the correlation V0M-CL0 removes also the outliers in the correlation between tracklets and V0M, as shown in Figure 1c and Figure 1d.

The last selection used to further reject the pile-up background is based on the position of the reconstructed primary vertex. High multiplicity events can contain two piled-up central collisions and in such conditions the vertex finding algorithm based on the reconstructed tracks fails to find the correct primary vertex. For this reason, the distribution of the z coordinate of the primary vertices shows some spikes and a large difference is visible between the reconstructed vertex position obtained with the SPD based method and the track based vertex finding algorithm (ΔV_z) as shown in Figure 2a. These discrepancies are ruled out using the resolution on the primary vertex reconstructed with tracks σ_{track} and SPD σ_{SPD} , and selecting only events where ΔV_z is less than $20\sigma_{track}$ and $10\sigma_{SPD}$. Furthermore the ΔV_z is required to be less than 0.2 cm. The effect of these selections is shown in Figure 2b. The event selections previously described and used in this analysis are summarized in Table 2.

¹The bunch crossing is defined as the instant when the two LHC beams cross at the ALICE interaction point. The time windows separating two bunch crossings are always multiple of 25 ns, that is the period of the LHC clock.

Event selection criteria		
Variable	Selection	Effect
$ V_z $	≤ 10 cm	uniform acceptance
Trigger	Minimum bias	
Multiple SPD vertices	reject with more than n contributors	pile-up rej.
$ V_{\text{OM}} - \text{CL0} $	$\leq 5\sigma$	pile-up rej.
$ V_{\text{OM}} - n_{\text{tracklets}}^{\text{SPD}} $	$\leq 5\sigma$	pile-up rej.
$ \Delta V_z $	$\leq 20\sigma_{\text{tracks}}, \leq 10\sigma_{\text{SPD}}$	pile-up rej.
$ \Delta V_z $	≤ 0.2 cm	pile-up rej.

Table 2: List of the event selections applied to the data sample used in this analysis. More details are given in the text.

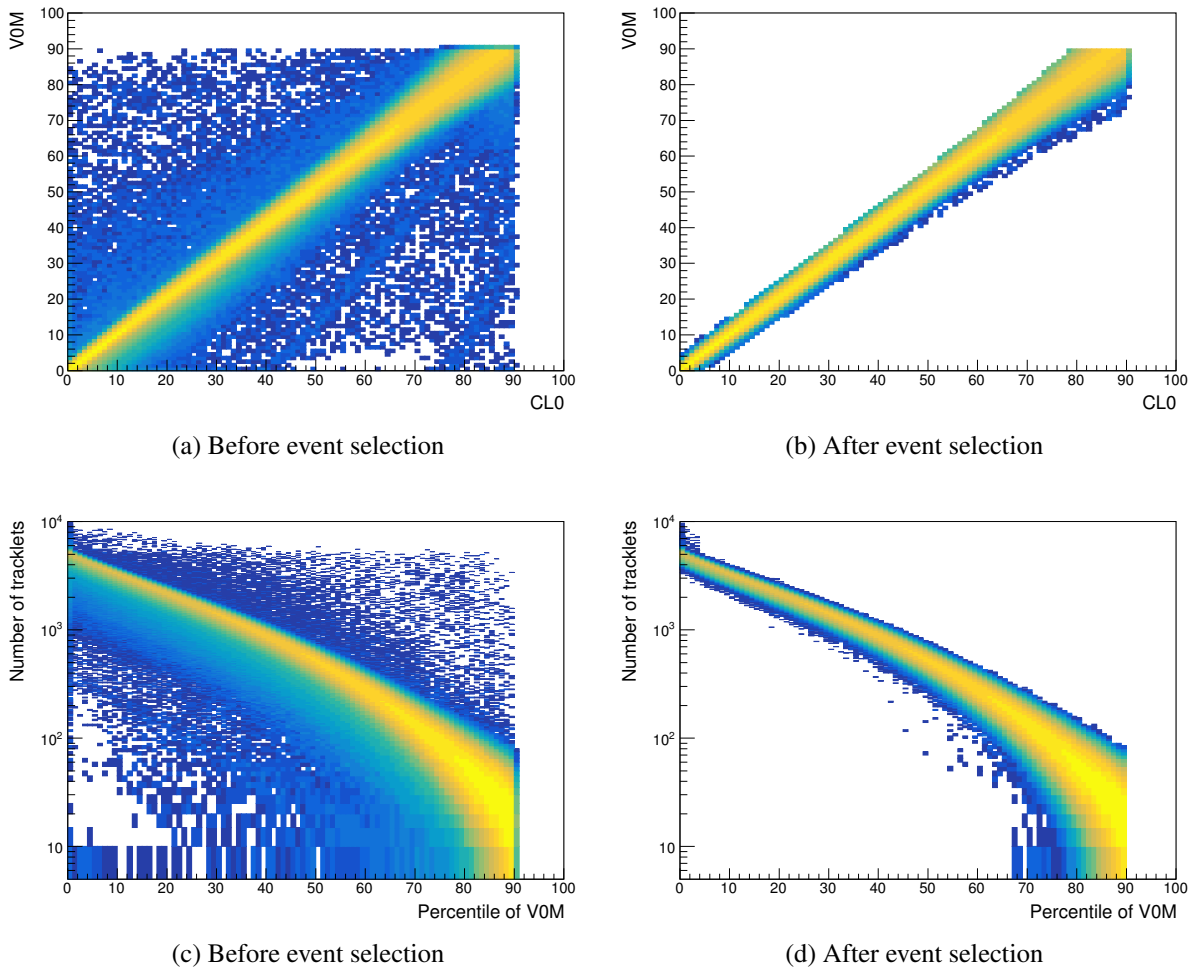


Fig. 1: Top: (a) correlation between the CL0 and VOM centrality estimators before event selection; (b) correlation between the CL0 and VOM centrality estimators after event selection. Bottom: (a) correlation between the number of SPD tracklets and the VOM estimator before event selection; (b) correlation between the number of SPD tracklets and the VOM estimator after event selection;

3.1 Selected data sample

After the offline event selection, the data sample consists of nearly 104 million Pb–Pb collisions at $\sqrt{s_{\text{NN}}}= 5.02$ TeV. The centrality percentile distribution for the 2015 data, which were collected with a

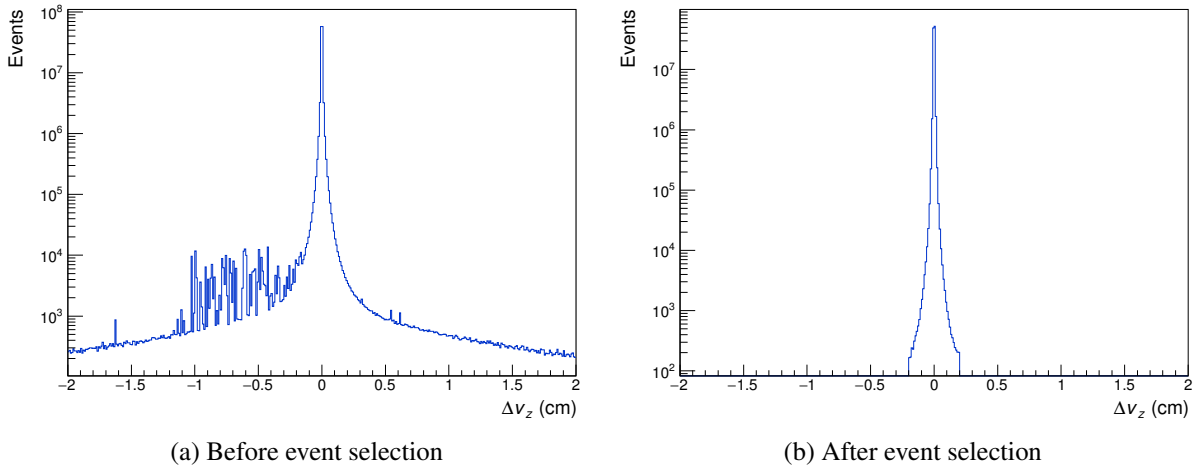


Fig. 2: Distribution of the distance between the primary vertex reconstructed with the tracks based and the SPD tracklets only vertex finding algorithm. The left plot shows the distribution before the event selection while the right plot shows the same distribution after the event selection.

161 minimum bias trigger, is flat in the range 0-90%, as shown in Figure 3.

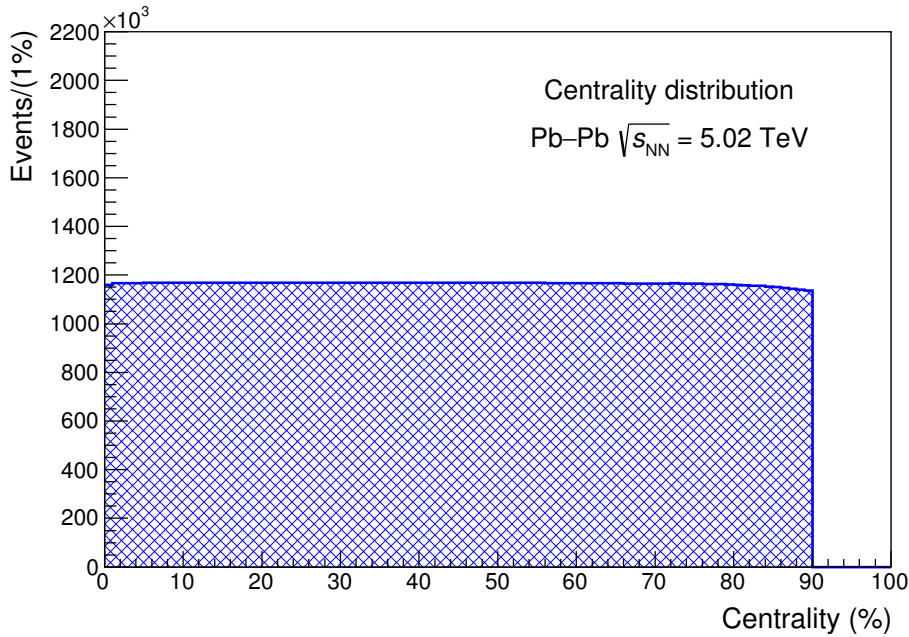


Fig. 3: V0M centrality percentile distribution for the 2015 data sample for the events satisfying the event selection criteria. Increasing the percentile means decreasing the collision centrality.

162 The whole collected statistics will be used for the $(\text{anti-})^3_\Lambda\text{H}$ lifetime measurement. With the available
 163 numbers and based on the idea to improve the published results [5], the 2015 data sample has been
 164 divided in 3 centrality intervals for the study of $(\text{anti-})^3_\Lambda\text{H}$ production yields: 0-10%, 10-30%, 30-50%.
 165 Moreover, since the ^3He spectra [6] have been measured in three different centrality classes (0-10%,
 166 10-40%, 40-90%), the $(\text{anti-})^3_\Lambda\text{H}$ production spectra have been measured using the events in the 10-40%
 167 centrality interval and this will allow the calculation of variables useful for the comparison with the
 168 theoretical models: the $^3\text{He}/^3_\Lambda\text{H}$ ratio and the S_3 parameter.

Centrality class observables						
Centrality	b_{\min} (fm)	b_{\max} (fm)	$\langle dN_{ch}/d\eta \rangle$	$\langle N_{part} \rangle$	Events	Analysis
0 - 10%	0.00	4.96	1765 ± 52	359 ± 4	11.6×10^6	dN/dy
10 - 30%	4.96	8.59	983 ± 25	226 ± 4	23.4×10^6	
30 - 50%	8.59	11.1	415 ± 14	108.6 ± 2	23.4×10^6	
10 - 40%	4.96	9.92	826 ± 22	194 ± 3	35×10^6	p_T spectra
0 - 90%	0.00	15.0	-	-	104.8×10^6	

Table 3: Centrality classes used in the analysis with their corresponding average values of the minimum (b_{\min}) and maximum (b_{\max}) impact parameter, the charged particles multiplicity ($\langle dN_{ch}/d\eta \rangle$) and the number of participating nucleons (N_{part}). These values are taken from [7, 8]. The last two columns report the total selected events and the measurement for each centrality class.

on-the-fly V^0 finder	
Variable	Value
track DCA_{PV}	> 1 mm
DCA_{tracks} at V^0	< 1.5 cm
$\cos(\theta_{pointing})$	> 0.9

Table 4: List of the selections applied to the V^0 candidate obtained with the on-the-fly V^0 finder algorithm [9] during the global reconstruction of the 2015 Pb–Pb collisions raw data.

The centrality classes are used to classify the collisions and are related to the overlap of the colliding nuclei, as presented in [7, 8]. Consequently, each centrality class is characterized by global event observables, as the number of participating nucleons (N_{part}) and the average charged particles multiplicity ($\langle dN_{ch}/d\eta \rangle$), which are related to the collision geometry. The relation of these observables with the centrality collision has been studied in detail by ALICE and the results are published in [7, 8]. Table 3 reports the most relevant event observables for the centralities used in this analysis. The values of (N_{part}) and ($dN_{ch}/d\eta$) are obtained with an average of the published results, following the same procedure adopted for other analyses in the collaboration, while b_{\min} and b_{\max} are obtained with the NBD-Glauber fit to the centrality distribution, which is shown in [8]. Moreover, the number of events for each centrality class is reported and will be used in the analysis of the production yields and spectra.

4 Hypertriton reconstruction

The aim of the analyses presented in this note is the study of the production of the $(\frac{3}{\Lambda}\bar{H})_{\Lambda}^3\text{H}$ and the measurement of its lifetime via the 2 body charged mesonic decay channels:

$$\frac{3}{\Lambda}\text{H} \longrightarrow {}^3\text{He} + \pi^- \quad \frac{3}{\Lambda}\bar{\text{H}} \longrightarrow {}^3\bar{\text{He}} + \pi^+ \quad (4)$$

Once the events are selected, the second step for all the analyses is the identification of $(\frac{3}{\Lambda}\bar{H})_{\Lambda}^3\text{H}$ candidates.

The method used for the reconstruction of the (anti-) $\frac{3}{\Lambda}\text{H}$ decay vertex is the on-the-fly V^0 finder algorithm [9]. As already mentioned, this algorithm runs only during the global reconstruction of the raw data. Since it is applied while the track is reconstructed, the track properties can be used, i.e. the full material and the magnetic field are known while the tracks are propagated, which is the main difference with respect to the offline algorithms. In order to reduce the combinatorial background already during the reconstruction, each V^0 candidate is selected by applying a set of loose cuts. In Table 4 the loose selections, applied during the global reconstruction of 2015 Pb–Pb collisions, are reported.

The V^0 candidates, which overcome these selections, are added to the V^0 candidates list in the output

of the reconstruction. Then specific selections are applied on the candidates at the analysis level. In the following, the selections of the daughter tracks and of the $(\bar{\Lambda}^0)^3\text{H}$ decay vertex are presented. A detailed study on the MC sample has been performed. First of all to check the correct identification and reconstruction of the $(\text{anti-})\Lambda^0$, since it is a charged particle and not neutral as expected in a candidate V^0 . Then also to tune the selections to be applied to the real data.

4.1 $(\text{Anti-})\Lambda^0$ candidates selection and PID

The identification of the $(\text{anti-})\Lambda^0$ candidates starts with the selection of the daughter tracks.

In order to use only the geometrical region where the ALICE experiment is able to perform a full tracking and to provide the best possible PID information, only tracks in the pseudorapidity region $|\eta| < 0.9$ are selected in these analyses. This requirements is mainly related to the TPC acceptance, since it is the main used detector. Moreover, to guarantee a track momentum resolution better than 5% and a TPC dE/dx resolution of 6%, the selected tracks are required to have at least 70 clusters in the TPC. The refit steps, which are the last part of the global tracking algorithm, are also performed in the reconstruction of the V^0 daughter tracks. Then the selected tracks are required to overcome successfully the TPC refit. In addition, the χ^2 per TPC clusters is computed in the track fitting procedure and is required to be less than 5. Finally the daughter tracks reconstructed as kink topology are rejected. Indeed this topology is defined for weak decay with a neutral daughter particle (e.g. $K^\pm \rightarrow \mu^\pm + \nu_\mu$). The aforementioned track selection criteria are applied to all the analyses presented in this analysis note and Table 5 summarises them.

Track selection criteria	
Variable	Selection
$ \eta $	≤ 0.9
$n_{TPCclusters}$	> 70
TPC refit	TRUE
$\chi^2/n_{TPCclusters}$	≤ 5
Kink topology	reject

Table 5: Summary of the track selections applied in the analyses of the 2015 data sample.

The following step is the identification of the daughter particles and it is performed using the TPC information on the specific energy loss. The most commonly used discriminating variable for PID is the $n\sigma$ variable, defined as the deviation of the measured signal from that expected for a species, in terms of detector resolution:

$$n\sigma = \frac{S_{measured} - S_{expected}^i}{\sigma_{expected}^i} \quad (5)$$

In Eq. 5, $S_{measured}$ is the measured signal for the candidate track, $S_{expected}^i$ is the expected signal for the species i and $\sigma_{expected}^i$ is the expected detector resolution for the same species i .

Figure 4 shows the specific energy loss for particles in the TPC active volume and the expected signal for pion (red line) and ^3He (black line), which are parameterized using the splines and are used in this analysis. The TPC response functions are parametrized for every data taking period and then included in the ALICE Offline framework, in order to be used for all the analyses.

The particle identification is performed track-by-track and applying a selection on the $n\sigma$ variable, as reported in Table 13. Pions are identified requiring a $n\sigma$ within ± 3 with respect to the expected π energy loss in the TPC given the momentum of the particle. Due to the contamination from kaons and protons the identification of pions can be performed up to ~ 1 GeV/c. At higher momenta the identification track-by-track is less trivial and could be improved requiring the matching with other PID detectors.

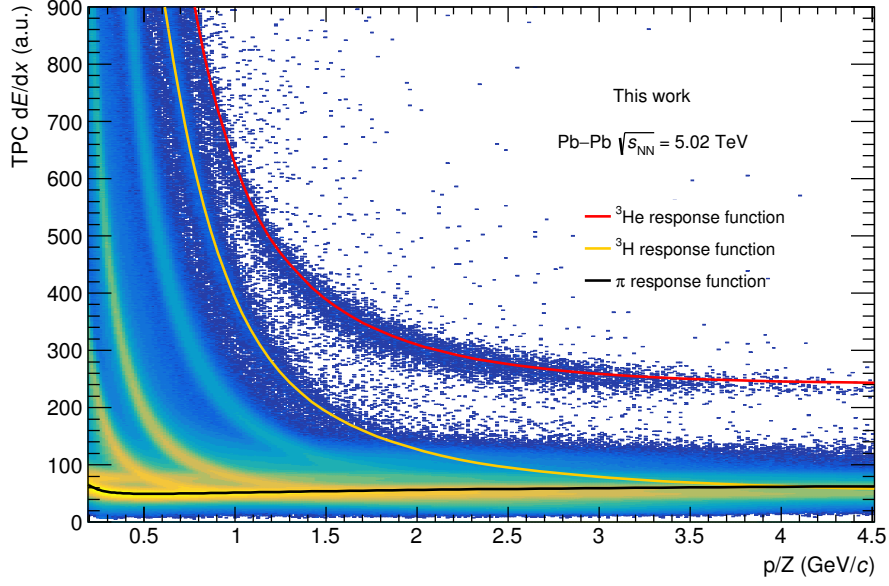


Fig. 4: Specific energy loss in the TPC active volume as a function of the particle rigidity in Pb–Pb collisions for the 2015 data sample. The solid lines represent the expected TPC response for pion (red) and ^3He (black).

Particle Identification		
Species	Variable	Selection
π	$ n\sigma_\pi $	≤ 3
^3He	$ n\sigma_{^3\text{He}} $	≤ 3
	$n\sigma_{^3\text{H}}$	> 0

Table 6: Selection applied for the identification of candidate π and ^3He using the specific energy loss in the TPC active volume.

However, the requirements of the identification in other detectors would reduce the final efficiency for the ^3H reconstruction. For these reasons, a study of the p_T distribution of the pions produced in the ^3H decay has been performed using MC events. The result is shown in Figure 5a where the maximum p_T for a π daughter is ~ 1 GeV/c. Consequently the candidate pions are required to have a p_T lying in the 0.2–1.2 GeV/c interval and the identification can be performed only with the TPC information.

Conversely, for the ^3He , that has charge $z = 2e$, the TPC can provide a clean identification up to high momenta. The explanation is given by the Bethe-Bloch [10]² formula for the specific energy loss, that depends on the square of z . Thus the ^3He is well separated from all the particle species with $z = 1e$ in a large momentum range. The only known species that could contaminate the ^3He signal in the TPC is the ^4He , but since its expected production rate is approximately 100 times smaller than the expected production of ^3H , it can be neglected in the present analysis work. In the low rigidity region, instead, the specific energy loss of the ^3He becomes similar to the one of the ^3H . As a consequence, the candidate ^3He are required to have the $n\sigma$ within ± 3 with respect to the expected ^3He TPC signal and the $n\sigma$ with respect to the expected ^3H TPC signal larger than 0. Furthermore, the p_T distribution of ^3He coming from the ^3H decay, shown in Figure 5b, suggests a selection on the minimum p_T of the ^3He at ~ 1.2 GeV/c. However, other analyses on nuclei production [11], performed in the ALICE Collaboration, showed that a large fraction of nuclei produced by secondary interaction has p_T smaller than 1.7–1.8 GeV/c. For this reason, the candidate ^3He are required to have p_T greater than 1.8 GeV/c.

²See the section “Experimental Methods and Colliders - Passage of particles through matter” of the PDG.

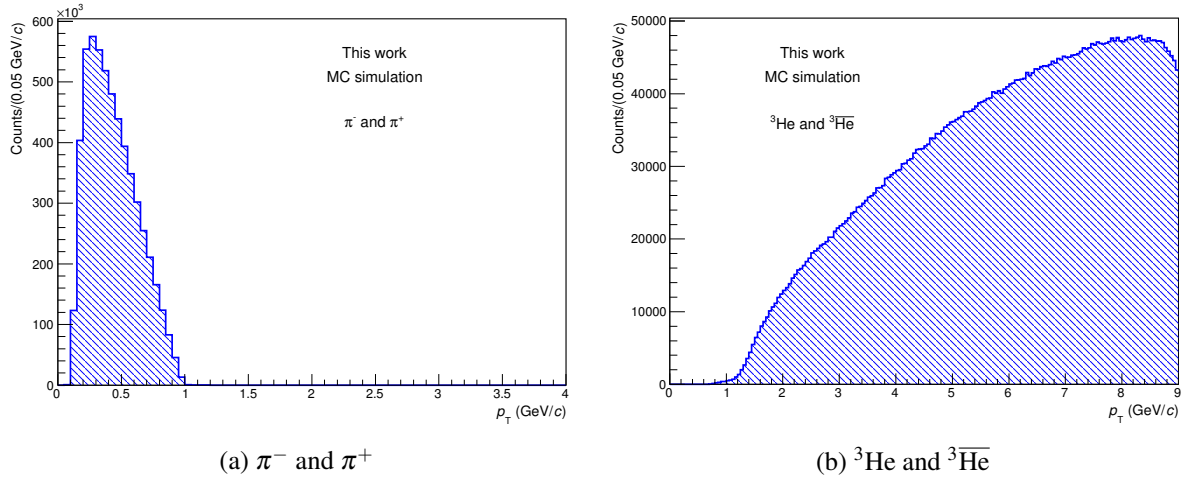


Fig. 5: Transverse momentum distribution of pions (left) and ${}^3\text{He}$ (right) from the $(\text{anti-}){}^3_\Lambda\text{H}$ decay. The distribution are obtained from the MC production.

4.2 Decay vertex selection

The last set of selections to identify $(\text{anti-}){}^3_\Lambda\text{H}$ candidates is performed on the reconstructed decay vertex. Indeed, the variables related to the topology and kinematics of the $({}^3_\Lambda\text{H}){}^3_\Lambda\text{H}$ candidate are evaluated during the decay vertex reconstruction. Thus it is possible to apply selections on these observables in order to maximize the $(\text{anti-}){}^3_\Lambda\text{H}$ signal and reject the combinatorial background. The latter is due to primaries π and ${}^3\text{He}$ which do not come from the $(\text{anti-}){}^3_\Lambda\text{H}$ decay and, however, satisfy the selections applied in the on-the-fly V^0 finder algorithm [9] (Table 4). A detailed study, using MC events, will allow to understand which additional selections can be required to further reduce the background.

Figure 6 shows a pictorial sketch of the ${}^3_\Lambda\text{H}$ two body decay and the topological observables used for the candidates selection.

The set of topological cuts include the distance of closest approach to the primary vertex for each candidate DCA_{PV}^i , which can be used to reject primary pions and ${}^3\text{He}$, and the distance of closest approach between the two daughters tracks at the secondary vertex DCA_{tracks} . Then, one of the most effective cuts for the rejection of the combinatorial background is the cosine of the pointing angle $\cos(\theta_{pointing})$. $\theta_{pointing}$ is the angle between the total momentum vector of the daughter pair and the straight line connecting the primary and secondary vertices.

The decay length is shown in Figure 6 with a solid straight line and represents the distance covered between the primary and secondary vertices. This observable is used to evaluate the lifetime of the candidate ct , which gives another topological cut. The definition of ct is:

$$ct = \frac{ML}{p} \quad (6)$$

where M is the nominal mass of the ${}^3_\Lambda\text{H}$ ($M = 2.991 \text{ GeV}/c^2$ [12]), L is the measured decay distance and p is the total momentum of the ${}^3_\Lambda\text{H}$ candidate. In particular, the decay distance is defined as:

$$L = \sqrt{(x_{SV} - x_{PV})^2 + (y_{SV} - y_{PV})^2 + (z_{SV} - z_{PV})^2} \quad (7)$$

where (x_{PV}, y_{PV}, z_{PV}) and (x_{SV}, y_{SV}, z_{SV}) are the coordinate of the primary and secondary vertex, respectively. For electrically neutral particles, the track length is the straight line between the production and the decay vertex. But for charged particles produced in the collision, the decay distance is equivalent to

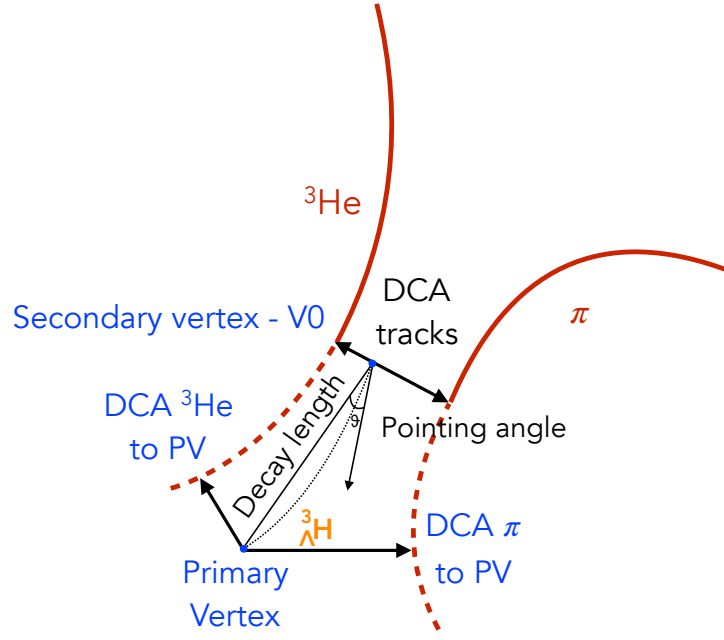


Fig. 6: Pictorial sketch of the $^3_\Lambda\text{H}$ two body decay. The observables which have been used to reduce the combinatorial background are reported on the figure.

the helix segment length because of the presence of the solenoidal magnetic field of L3. The definition of the length of the helix segment is:

$$\text{Helix length} = \sqrt{(\text{Ark length})^2 + (z_{\text{SV}} - z_{\text{PV}})^2} \quad (8)$$

with

$$\text{Ark length} = 2R \cdot \arcsin \left(\sqrt{\frac{(x_{\text{SV}} - x_{\text{PV}})^2 + (y_{\text{SV}} - y_{\text{PV}})^2}{4R^2}} \right) \quad (9)$$

where R is the curvature radius of the charge track, defined as:

$$R = \frac{p_T}{qB} = \frac{p_T}{B} \cdot \frac{10}{3} \quad (10)$$

where p_T is given in GeV/c, B in Tesla and R in meter. For two candidates with p_T equal to 2 and 10 GeV/c, the corresponding curvature radii are ~ 13 m and ~ 67 m, respectively.

The correlation between the length measured with the helix and straight line approach has been studied and the result is shown in Figure 7a. The dashed orange line corresponds to the ideal case where the two lengths are exactly the same and it is visible that there are no differences between the two approaches. As a consequence the decay distance can be evaluated following Eq. 7.

Two additional observables related to the kinematics of the (anti-) $^3_\Lambda\text{H}$ candidate are used in the selection criteria: the rapidity y and the transverse momentum p_T .

In order to measure the $^3_\Lambda\text{H}$ production yield and spectrum in the mid-rapidity region, the candidates are required to have $|y| < 0.5$.

The transverse momentum of the candidate $^3_\Lambda\text{H}$ is required to be larger than 2 GeV/c. Figure 7b shows the p_T distribution of (anti-) $^3_\Lambda\text{H}$ reconstructed in the MC production and few of them are reconstructed in the p_T region below 2 GeV/c. On the other hand, that p_T range is largely contaminated by candidate obtained

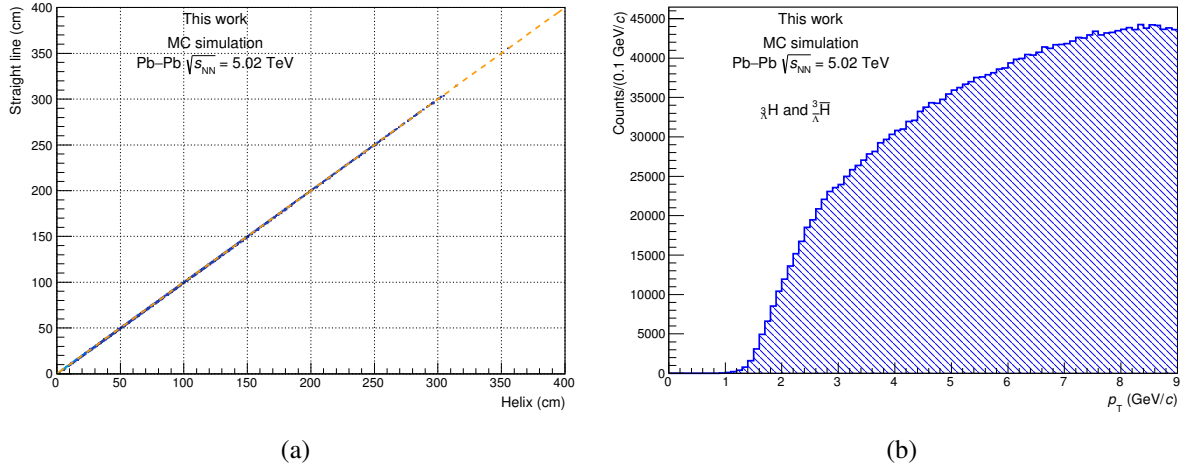


Fig. 7: (Left) Helix vs straight line length (cm) for ${}^3_{\Lambda}\text{H}$ candidates. The dashed orange line corresponds to equal lengths. (Right) p_T distribution of the reconstructed ${}^3_{\Lambda}\text{H}$ obtained using MC events.

pairing pions and ${}^3\text{He}$ from secondary interaction. Moreover, this selection has the advantage to exclude the transverse momentum range where the reconstructed p_T is affected by the mis-assignment of the mass hypothesis to the ${}^3\text{He}$ candidate. Indeed, during the track fitting step of the reconstruction, the mass hypothesis of the tracked particle is used to keep into account the particle energy loss while traversing the material. The mass hypothesis is chosen among the particle whose expected dE/dx is compatible with the one measured with the track. However, during the reconstruction the selection on the expected energy loss is loose ($|\ln\sigma| < 15$). As a consequence, some ${}^3\text{He}$ candidate can be reconstructed with the mass hypothesis of ${}^4\text{He}$ or ${}^3\text{H}$ and this lead to an imprecise reconstruction of the ${}^3\text{He}$ momentum for $p_T \leq 1.8$ GeV/c. Figure 8a shows the relative difference between the generated p_T^{MC} and reconstructed p_T^{reco} transverse momentum of the ${}^3\text{He}$ and there are large deviations due to the different mass hypothesis. The effect on the reconstructed p_T of the ${}^3_{\Lambda}\text{H}$ is mainly in the low p_T region but is strongly suppressed with the aforementioned selection on the ${}^3\text{He}$ p_T . Figure 8b shows the relative difference for the $({}^3_{\Lambda}\bar{\text{H}}){}^3_{\Lambda}\text{H}$ transverse momentum. The candidate ${}^3\text{He}$ daughter are selected as previously mentioned and there is a small relative difference of $\sim 2\text{-}3\%$ between 2 and 2.2 GeV/c. To recover the missed momentum fraction, a fit to the distribution has been performed with the following formula:

$$f(p_T^{reco}) = a - b \cdot \exp(-c \cdot p_T^{reco}) \quad (11)$$

and the resulting parameterisation has been used to apply a track-by-track correction to the reconstructed (anti-) ${}^3_{\Lambda}\text{H}$ transverse momentum.

The analysis presented in this note uses the on-the-fly V^0 finder algorithm, which was developed for the reconstruction of neutral particle decays. For this reason, preliminary studies on the MC sample have been performed to check the reconstruction of the ${}^3_{\Lambda}\text{H}$ and the effect of the selection criteria previously introduced.

Baseline selections which have already been studied and tuned properly are the event selections, the track selections, the particle identification and the p_T ranges for the reconstructed decay products and $({}^3_{\Lambda}\bar{\text{H}})\text{hypertriton}$.

The focus of these preliminary studies is on the DCA between the daughters tracks $\text{DCA}_{{}^3\text{He},\pi}$, the DCA of the π track to the primary vertex $\text{DCA}_{p_V}^{\pi}$, the cosine of the pointing angle $\cos(\theta_{\text{pointing}})$ and the lifetime ct . A detailed presentation on the studies performed on the MC simulation was given at NuclEx PAG meeting on the 21st December 2016 and here is the link <https://indico.cern.ch/event/595860/>

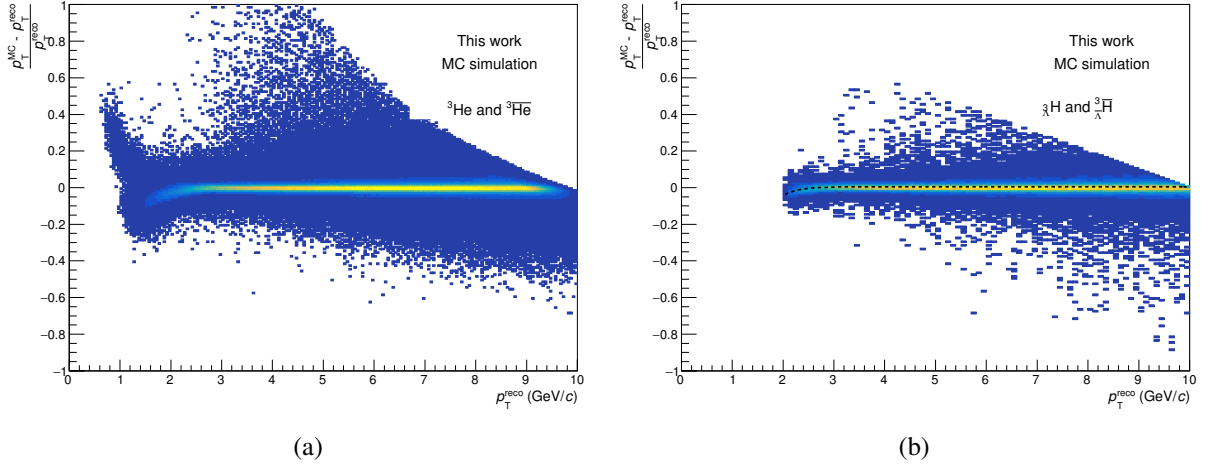


Fig. 8: Relative difference between generated (p_T^{MC}) and reconstructed (p_T^{reco}) transverse momentum as a function of p_T^{reco} for ${}^3\text{He}$ (left) and ${}^3_{\Lambda}\text{H}$ (right). The dashed black line on the right plot corresponds to the correction applied to the reconstructed (anti-) ${}^3_{\Lambda}\text{H}$ p_T .

5 Production yields vs centrality

The study of the production as a function of the collision centrality is crucial for testing and constraining the model predictions. In this section the determination of the production yields per rapidity dN/dy is presented for three different centrality classes (0–10%, 10–30%, 30–50%).

5.1 Raw yields extraction vs centrality

The candidates ${}^3_{\Lambda}\text{H}$ and ${}^3_{\Lambda}\bar{\text{H}}$, used in the determination of the raw yield, are chosen separately applying the selection criteria described in the previous chapter. Table 7 reports the set of cuts applied in this analysis for the three centrality classes. The requirements have been determined after an accurate MC study of the effect of the different selection criteria. Only in the 0–10% centrality class, pion tracks are required to have a DCA to the primary vertex $\text{DCA}_{p_V}^{\pi}$ larger than 0.2 cm. The reason for this additional selection in the most central collisions is related to the large number of primary pions (~ 2000) produced in those collisions.

Candidate selections			
	0–10%	10–30%	30–50%
π p_T (GeV/c)	0.2–1.2	0.2–1.2	0.2–1.2
${}^3\text{He}$ p_T (GeV/c)	≥ 1.8	≥ 1.8	≥ 1.8
$\text{DCA}_{p_V}^{\pi}$ (cm)	≥ 0.2	-	-
DCA_{tracks} (cm)	< 0.7	< 0.7	< 0.7
ct (cm)	> 2	> 2	> 2
$\cos(\theta_{pointing})$	≥ 0.995	≥ 0.995	≥ 0.995
$ y $	≤ 0.5	≤ 0.5	≤ 0.5

Table 7: Set of cuts applied for the selection of ${}^3_{\Lambda}\text{H}$ and ${}^3_{\Lambda}\bar{\text{H}}$ candidates in the three centrality classes.

The invariant mass distributions for the candidates selected with the aforementioned criteria are reported in Figure 9, on the left for the ${}^3_{\Lambda}\text{H}$ and on the right for the ${}^3_{\Lambda}\bar{\text{H}}$. The distributions are also divided in the three centrality class 0–10% (top), 10–30% (middle) and 30–50% (bottom). The fitting function used for the signal extraction is the sum of two probability density functions, a Gaussian for the signal and a second degree polynomial for the background and it is drawn with a blue curve. The parameters of the

background component are determined with a fit to the sidebands distribution, which corresponds to the $[-9\sigma, -4\sigma]$ and $[+4\sigma, +9\sigma]$ intervals from the mean of the Gaussian, and is represented with a red dashed line. The sidebands are chosen in order to be far from the region where the signal is expected and to fit the combinatorial background only. The normalization of the fit function is kept into account with two parameters N_{sig} and N_{bkg} , which corresponds to the signal and background counts, respectively. The fit function is defined as:

$$\text{p.d.f.}(m) = N_{sig} \cdot \text{p.d.f.}_{sig}(m|\mu, \sigma) + N_{bkg} \cdot \text{p.d.f.}_{bkg}(m|a_i) \quad (12)$$

where m is the invariant mass, μ and σ are the mean and width of the Gaussian, respectively, while a_i are the parameters of the polynomial.

In the centrality class 30–50% the statistics is very low, by a factor 3 compared to the 0–10% class, and the signal extraction depends on the outcome of the fit to the distribution. For this reason, a first fit is performed on the invariant mass distribution obtained from the sum of matter and anti-matter. The σ of the Gaussian is evaluated from the result of the fit. Then the signal extraction of matter and anti-matter separately is performed fixing the σ of the fitting function to the previously found value.

The mean (μ) and the width (σ) of the Gaussian distribution are evaluated in the fit procedure and the first one is compared, for all the three centrality classes, with the experimental mass value of the $(\frac{3}{\Lambda}\bar{H})\frac{3}{\Lambda}H$ measured by the ALICE [5] and STAR [13] experiments. Figure 10a and 10b show this comparison for $\frac{3}{\Lambda}H$ (a) and $\frac{3}{\Lambda}\bar{H}$ (b), respectively, and all the mean values are in agreement within the uncertainties with the other experimental results.

The mean values from the $\frac{3}{\Lambda}\bar{H}$ invariant mass fit in the three analysed centralities are comparable and the same can be observed for the $\frac{3}{\Lambda}H$. On the other hand the $\frac{3}{\Lambda}\bar{H}$ mass is slightly higher than the one of the $\frac{3}{\Lambda}H$, even if in agreement with previous experimental values. Still more important is the comparison between the σ which will be used to estimate the raw yields and are compatible between matter and antimatter in the different centralities.

The counts of signal S (raw yield) and background B are obtained from the integral of the respective component of the fitting function in the range $\pm 3\sigma$ with respect to the mean value of the Gaussian. Thus it is possible to calculate the S/B and the significance $S/\sqrt{S+B}$ for the signal extracted. The increase of the signal over background ratio (S/B) from the 0–10% to the 30–50% is due to the reduction of the combinatorial background as can be also seen in Figure 9. Indeed, the combinatorial background is expected to scale also with the charged particle multiplicity, which decreases going from central to peripheral collisions. A summary of the fit results and signal extraction for $\frac{3}{\Lambda}H$ and $\frac{3}{\Lambda}\bar{H}$ in the three analysed centrality classes is reported in Table 8 and 9, respectively.

As a general rule, the raw yield estimate is statistically significant if the significance is larger than 3, which corresponds to the 99.7% of the integral of a Gaussian probability density function (p.d.f.). However the signals extracted for $\frac{3}{\Lambda}H$ in the 10–30% and 30–50% centrality classes are slightly below the threshold, precisely 4% and 11% off the 3σ . As a crosscheck, the signals are extracted from the merged invariant mass distributions of matter and anti-matter and are compared with the sum of the obtained raw yields. The outcome of the check is that in both cases the significance is larger than 3 and the raw yields of 88 ± 21 in 10–30% and 46 ± 16 in 30–50% are compatible with sum of the signals extracted separately. Thus, also the raw yields of the $\frac{3}{\Lambda}H$ in 10–30% and 30–50% are used to study the production in the semi-central collisions, despite their significances.

	$\frac{3}{\Lambda}\text{H}$		
	0–10%	10–30%	30–50%
mean (GeV/c^2)	2.9911 ± 0.0007	2.9916 ± 0.0009	2.9901 ± 0.0009
width (GeV/c^2)	0.0023 ± 0.0005	0.0027 ± 0.0003	0.0021 ± 0.0007
χ^2/NDF	1.60	1.36	0.89
S/B	0.22	0.19	0.42
Significance (3σ)	3.34	2.88	2.65
Raw yield	69 ± 16	49 ± 13	27 ± 8

Table 8: From top: mean, width, χ^2/NDF , S/B and significance obtained from the fit to the $\frac{3}{\Lambda}\text{H}$ invariant mass distributions in the three centrality classes. Raw yields are obtained as the integral of the signal function in $\pm 3\sigma$ with respect to the mean value.

	$\frac{3}{\Lambda}\bar{H}$		
	0–10%	10–30%	30–50%
mean (GeV/c^2)	2.9923 ± 0.0009	2.9929 ± 0.0007	2.9923 ± 0.0007
width (GeV/c^2)	0.0029 ± 0.0008	0.0027 ± 0.0005	0.0021 ± 0.0005
χ^2/NDF	1.38	1.26	1.93
S/B	0.26	0.26	0.85
Significance (3σ)	3.33	3.07	3.40
Raw yield	58 ± 12	42 ± 12	22 ± 7

Table 9: From top: mean, width, χ^2/NDF , S/B and significance obtained from the fit to the $\frac{3}{\Lambda}\bar{H}$ invariant mass distributions in the three centrality classes. Raw yields are obtained as the integral of the signal function in $\pm 3\sigma$ with respect to the mean value.

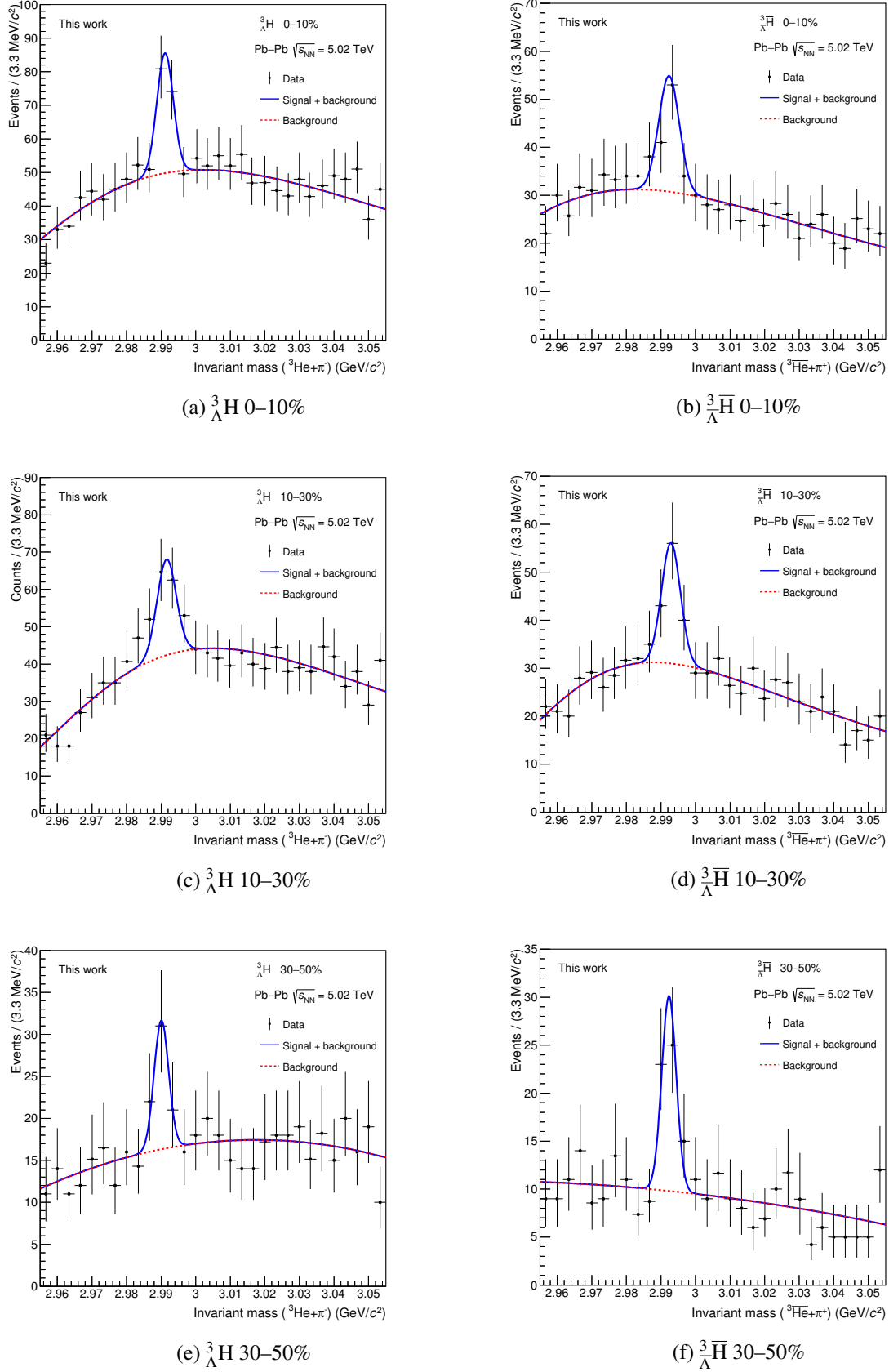


Fig. 9: Invariant mass distributions of ${}^3_{\Lambda}\text{H}$ (left) and ${}^3_{\Lambda}\bar{\text{H}}$ (right) in the 0–10% (top), 10–30% (middle) and 30–50% (bottom) centrality class. The blue curve is the fit function, sum of signal background (Gaussian + pol2), and the red dashed line is the background component.

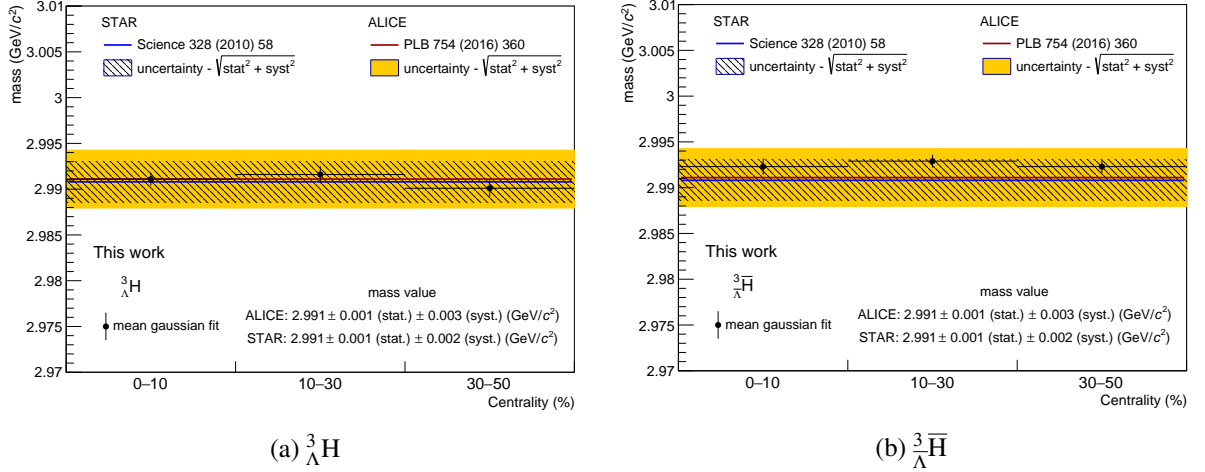


Fig. 10: Mean values with their uncertainties obtained from the fit to the $\frac{3}{\Lambda}\text{H}$ (a) and $\frac{3}{\Lambda}\bar{H}$ (b) invariant mass distributions compared with the experimental mass value measured by STAR [13] and ALICE [5].

5.2 Efficiency correction

The measured raw yields are biased by inefficiencies in the ALICE detectors. For instance, the active area of the experiment is not hermetic by design (e.g. sector edges of the TPC) or, sometimes, parts of the detectors might be switched off during some periods of the data taking periods (e.g. TPC readout chambers excluded during some runs because unstable).

It is possible to correct for the finite efficiency and acceptance using a MC simulation where the full geometry and the real data taking conditions are reproduced. The MC production used for this analysis has been described in detail in Sec. 2.2. The number of particles crossing the detectors and their kinematics observables are known when using a MC simulation and the efficiency \times acceptance can be computed as:

$$Efficiency \times Acceptance(p_T) = \frac{N_{rec}(p_T)}{N_{gen}(p_T)} \quad (13)$$

where N_{gen} is the number of $(\frac{3}{\Lambda}\bar{H})_{\Lambda}^3\text{H}$ generated in the azimuthal region $0 \leq \phi < 2\pi$ and in the rapidity range $|y| < 0.5$, while N_{rec} is the number of $(\frac{3}{\Lambda}\bar{H})_{\Lambda}^3\text{H}$ that satisfies the selection criteria summarised in Table 7. The efficiency \times acceptance is evaluated for $\frac{3}{\Lambda}\text{H}$ and $\frac{3}{\Lambda}\bar{H}$ separately as a function of the transverse momentum and it is shown in Figure 11a and 11b. The distributions are obtained in the centrality classes used in the analysis to check if the different occupancies of the detector play a role in the reconstruction performance. Moreover they are evaluated in narrow p_T intervals to take into account the dependence on the transverse momentum of the particles. In particular, the efficiency for the candidates reconstruction in 0–10% lower since there is the additional cut on the DCA_{PV}^{π} .

Since the extracted $\frac{3}{\Lambda}\text{H}$ and $\frac{3}{\Lambda}\bar{H}$ raw yields are p_T -integrated in the range 2–9 GeV/c (see Table 7), the efficiency correction estimate has to be provided also p_T -integrated in the same interval. Practically, it is obtained as a weighted average of the efficiency \times acceptance distribution from 2 to 9 GeV/c following:

$$Efficiency \times Acceptance = \frac{\sum_{p_T=2}^9 w_{p_T} \cdot \varepsilon(p_T)}{\sum_{p_T=2}^9 w_{p_T}} \quad (14)$$

where $\varepsilon(p_T)$ is the efficiency for a given p_T , as in Eq. 13, while the weight w_{p_T} is taken from the Blast-Wave [21] distributions of the ^3He [6], shown in Figure 12. The reason for this choice is related to the fact that the ^3He mass is much closer to that one of the $\frac{3}{\Lambda}\text{H}$ than the other light hadrons (e.g. π , K, p). In particular the ^3He Blast-Wave distributions are obtained in the 0–10% (blue), 10–40% (red) and 40–90%

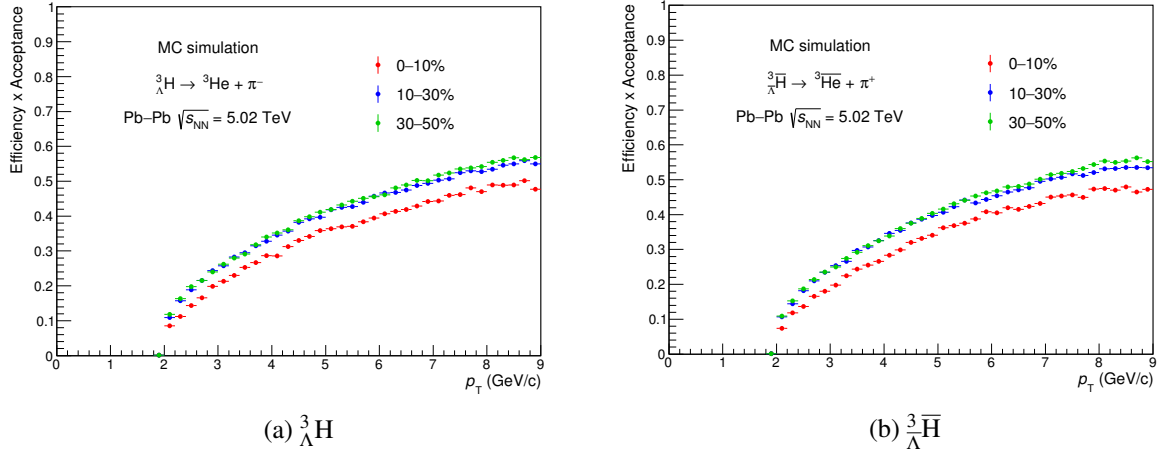


Fig. 11: Efficiency \times acceptance as a function of p_T for ${}^3_\Lambda\text{H}$ (a) and ${}^3_\Lambda\bar{\text{H}}$ (b) in the three centrality classes 0–10% (red), 10–30% (blue) and 30–50% (green).

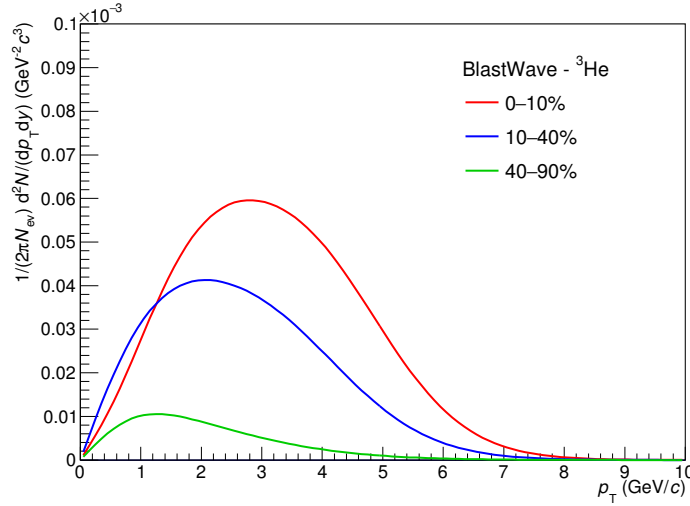


Fig. 12: Blast-Wave distributions from the analysis of the ${}^3\text{He}$ production in three centrality classes 0–10% (blue), 10–40% (red) and 40–90% (green) [6].

(green) centrality classes and are used in the average computation of the $({}^3_\Lambda\bar{\text{H}}){}^3_\Lambda\text{H}$ efficiencies in 0–10%, 10–30% and 30–50%, respectively.

The efficiency \times acceptance values, obtained from the weighted average, are reported in Table 10 and are used to correct the raw yields previously extracted of the ${}^3_\Lambda\text{H}$ and the ${}^3_\Lambda\bar{\text{H}}$ reported in Table 8 and 9.

Efficiency \times Acceptance			
	0–10%	10–30%	30–50%
${}^3_\Lambda\text{H}$	25.3 %	27.6 %	25.4 %
${}^3_\Lambda\bar{\text{H}}$	24.5 %	27.1 %	24.7 %

Table 10: Efficiency \times acceptance for ${}^3_\Lambda\text{H}$ (top) and ${}^3_\Lambda\bar{\text{H}}$ (bottom) in the three centrality classes. More details on their evaluation in the text.

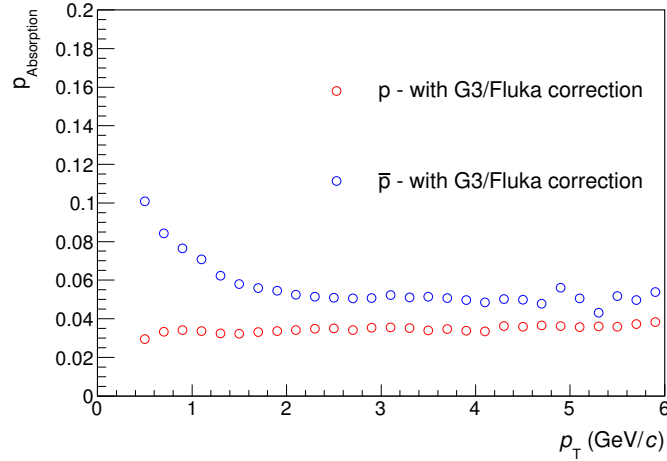


Fig. 13: Absorption probability of protons (red) and anti-protons (blue) from [14]

5.3 Absorption correction

GEANT3 is the transport code used in the MC productions used to finalize the analysis and it does not take into account the interaction of $\bar{\Lambda}^3\text{H}$ and $\Lambda^3\bar{\text{H}}$ with the material. This can be deduced from the efficiency distributions of $\bar{\Lambda}^3\text{H}$ and $\Lambda^3\bar{\text{H}}$ in Figure 11a and 11b, which have the same trend and magnitude.

In order to estimate the correction for the absorption of $\bar{\Lambda}^3\text{H}$ and $\Lambda^3\bar{\text{H}}$ an empirical approach has been adopted and the key elements for this evaluation are the absorption probabilities of $(\bar{\Lambda}^3\text{H})^3\text{H}$ and of $(\bar{\Lambda}^3\text{He})^3\text{He}$. In this analysis, as already done for the published results [5], the absorption indicates all those interactions which do not allow the $(\bar{\Lambda}^3\text{H})^3\text{H}$ and its daughters to reach the TPC and, thus, to be identified.

Since the interaction cross section for (anti-)nuclei is barely known and is missing for the (anti-)hypernuclei, the starting point for this calculation is the absorption probability of p and \bar{p} measured by the ALICE Collaboration [14]. Figure 13 shows the fractions of protons (red) and anti-protons (blue) which do not reach the TPC ($p_{\text{Absorption}}$) and they are computed using a MC simulation using GEANT3 with the Fluka correction. The latter one is a correction applied to the parameterisation of the inelastic cross section for p-A and \bar{p} -A interaction, in the MC simulation. Indeed, in [15], it is shown that GEANT3 significantly overestimates the measured inelastic cross-sections, while FLUKA describes the data very well. Thus, the FLUKA results are used to account for the difference p and \bar{p} cross sections. More details can be found in [15]. The probability of a proton to be absorbed can be written as:

$$p_{\text{Absorption}} = 1 - e^{-n_0 \sigma L} \quad (15)$$

where n_0 is the number of scattering center proportional to the density of the target, σ is the interaction cross-section of the projectile on the target and L is the path length of the projectile. In the probabilities reported in Figure 13 L is equal to the distance between the primary vertex (PV) and the TPC wall (TPC) that is 80 cm. Thus, it can be evaluated the absorption probability for p and \bar{p} as a function of the distance from the primary vertex, as shown in Figure 14a and 14b. They are evaluated for p (a) and \bar{p} (b) dividing the distance of 80 cm in intervals with width $\Delta L = 1$ cm and assigning, for each ΔL and each p_T , 1/80 of the total absorption probability previously shown (Figure 13). The material density ρ , taken from the results on the photon conversion analysis performed in ALICE [3], is also included in the calculation. These two dimensional distributions are used as baseline for the next steps.

The absorption probability of the $(\bar{\Lambda}^3\text{He})^3\text{He}$ is calculated from that one of the $(\bar{p})p$ and assuming the same

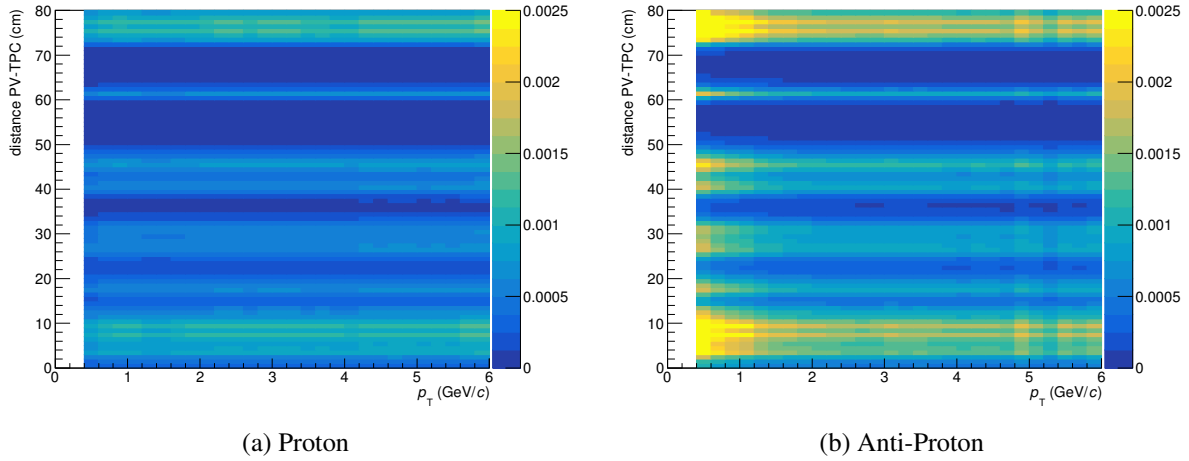


Fig. 14: Absorption probability as a function of the distance between the primary vertex and the TPC for protons (a) and anti-protons (b).

distribution for protons and neutrons. Thus the probability to absorb the ^3He can be written as:

$$p_{\text{Absorption},^3\text{He}} = 1 - p_{\text{NotAbsorption},p}^3 \quad (16)$$

where $p_{\text{NotAbsorption},p}$ is defined as $1 - p_{\text{Absorption},p}$, according to the definition of binomial distribution, and $p_{\text{Absorption},p}$ is the proton absorption probability (Eq. 15).

The evaluation of the absorption probability for the $(\bar{\Lambda}^3\text{H})_{\Lambda}^3$ is performed adopting a similar approach, but, in this case, to take into account the small Λ separation energy, the $^3_{\Lambda}\text{H}$ cross-section is increased by 50% with respect to the one of the ^3He . This choice was already done in the published result [5] and it is based on the calculation of the $^3_{\Lambda}\text{H}$ absorption cross-section on ^{238}U [16] and its ratio with the extrapolated ^3He cross-section [17] on the same target. The probability can be written as:

$$p_{\text{Absorption},^3_{\Lambda}\text{H}} = 1 - e^{-1.5n_0\sigma_{^3\text{He}}L} \quad (17)$$

The absorption probabilities of the ^3He and the $^3_{\Lambda}\text{H}$ are finally used to compute the probability not to observe an $(\bar{\Lambda}^3\text{H})_{\Lambda}^3$ in the path between the primary vertex and the TPC inner wall. This probability is defined as:

$$p_{\text{NotObserve}_{\Lambda}^3\text{H}}^{(\text{PV}-\text{TPC})} = p_{\text{Absorption}_{\Lambda}^3\text{H}}^{(\text{PV}-\text{SV})} + \left(1 - p_{\text{Absorption}_{\Lambda}^3\text{H}}^{(\text{PV}-\text{SV})}\right) \cdot p_{\text{Absorption}_{^3\text{He}}}^{(\text{SV}-\text{TPC})} \quad (18)$$

where (PV-SV) is the distance between the primary vertex and the decay vertex, while (SV-TPC) is the distance between the decay vertex and the TPC inner wall. Finally the probability to observe the $^3_{\Lambda}\text{H}$, which is used as correction factor for the absorption, is obtained as:

$$p_{\text{Observe}_{\Lambda}^3\text{H}}^{(\text{PV}-\text{TPC})} = \left(1 - p_{\text{NotObserve}_{\Lambda}^3\text{H}}^{(\text{PV}-\text{TPC})}\right) \quad (19)$$

The probability to observe an $(\bar{\Lambda}^3\text{H})_{\Lambda}^3$ depends on the distance between the primary vertex and the decay vertex (PV-SV), as can be deduced from Eq. 18. Thus, the probability has been evaluated for different distances (PV-SV) and the two extreme cases, corresponding to $\text{PV-SV} = 1$ cm and $\text{PV-SV} = 79$ cm, are shown in Figure 15a and 15b for the $^3_{\Lambda}\text{H}$ and the $^3_{\Lambda}\bar{\text{H}}$, respectively. The black curve corresponds to a decay vertex inside the beam pipe ($\text{PV-SV} = 1$ cm), while the blue curve corresponds to an $(\bar{\Lambda}^3\text{H})_{\Lambda}^3$ which travels without decaying through the whole ITS ($\text{PV-SV} = 79$ cm). The absorption correction used

in the analyses is assessed with an average between the two limiting cases and corresponds to the orange curve in Figure 15.

The probability to observe an $\frac{3}{\Lambda}\bar{H}$ increases from 0.65, at low p_T , to a constant value around 0.80 at high p_T , while the same probability for the $\frac{3}{\Lambda}H$ is flat around 0.85. The probability for p_T below 0.4 GeV/c is 1 both for matter and anti-matter and is due to the fact that the absorption probability for p and \bar{p} is unmeasured in that range. However, this low p_T range is not relevant for the transverse momentum ranges considered in this analysis. Indeed the candidates $(\frac{3}{\Lambda}\bar{H})\frac{3}{\Lambda}H$ are selected between 2 and 9 GeV/c and this means to use the absorption correction in the $(\bar{p})p$ p_T range from 0.65 to 3 GeV/c, assuming the proton p_T as one third of the $\frac{3}{\Lambda}H$ p_T .

Thanks to the probability to observe a $\frac{3}{\Lambda}H$ and an $\frac{3}{\Lambda}\bar{H}$, just obtained, the correction factor can be calculated. In particular, since the production yields are extracted p_T -integrated in the range 2-9 GeV/c, the absorption correction is evaluated with a weighted average of the distributions in the corresponding proton p_T range previously discussed. The weights are taken from the ^3He Blast-Wave already introduced in Sec. 5.2 and have been used following the same approach adopted in the efficiency calculation. The results of the weighted average are reported, for the three centrality classes of this analysis, in Table 11. These values are used to correct for the absorption by dividing the measured raw yields for the corresponding correction factor.

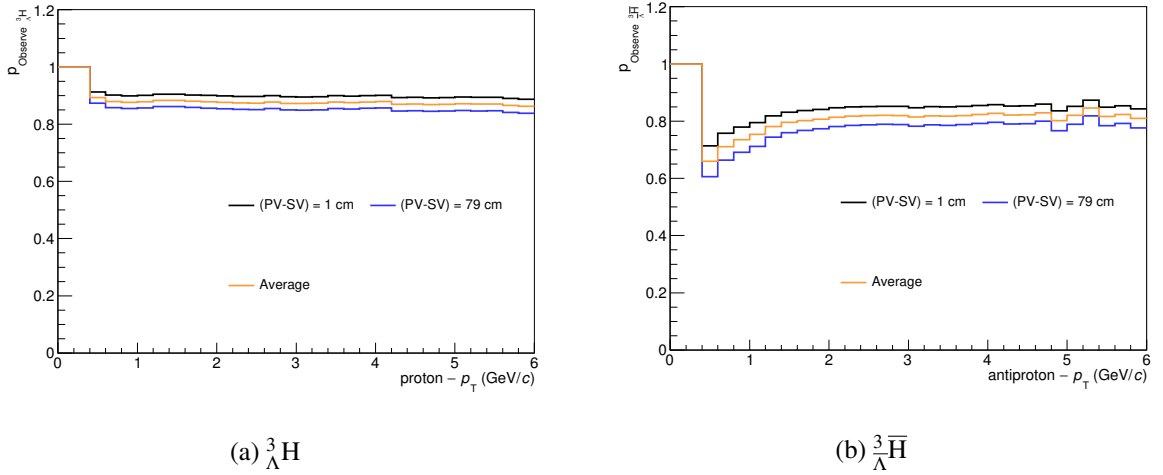


Fig. 15: Probability to observe a $\frac{3}{\Lambda}H$ (a) and an $\frac{3}{\Lambda}\bar{H}$ (b) as a function of the $(\bar{p})p$ p_T . The black and blue curves correspond to a distance between primary and secondary vertices of 1 cm and 79 cm respectively. The orange curve is the average between the two distributions and it is the final correction.

Absorption correction			
	0–10%	10–30%	30–50%
$\frac{3}{\Lambda}H$	87.96 %	87.95 %	87.91 %
$\frac{3}{\Lambda}\bar{H}$	76.2 %	75.4 %	74.4 %

Table 11: Probability to observe the $\frac{3}{\Lambda}H$ (top) and the $\frac{3}{\Lambda}\bar{H}$ (bottom) in the three centrality classes. More details on their evaluation in the text.

5.4 Systematics uncertainties

The accurate study of the systematic uncertainties is a fundamental part, especially in this analysis where the combinatorial background is very large and, thus, the applied selections could introduce systematic effects. The main sources and the corresponding checks can be classified in four groups:

1. the absorption correction, done by varying the assumption on the $(\frac{3}{\Lambda}\bar{H})\frac{3}{\Lambda}H$ cross-section and using the $p_{Observe}$ distributions of different (PV-SV) distance;
2. the efficiency \times acceptance, performed with different weights and taking into account the uncertainty on the material budget;
3. the selections criteria for the candidates and on the method adopted for the raw yield extraction;
4. the unknown $\frac{3}{\Lambda}H$ p_T -shape for the extrapolation of the yield in the unmeasured p_T regions.

These sources of systematic uncertainties are common to all the analyses presented in this note. Thus they will be described in detail in this section, while in the following sections the results on the checks will be discussed.

The absorption correction is obtained with an empirical approach and it is based on two main assumptions, as described in Sec 5.3. The systematic uncertainty related to the usage of an average correction is evaluated using the probability to observe an $(\frac{3}{\Lambda}\bar{H})\frac{3}{\Lambda}H$ which decays in one case in the beam pipe (PV-SV = 1 cm) and in the other case close to the TPC (PV-SV = 79 cm). The raw yields are corrected separately with these two probabilities and the semi-difference between the corrected yields is taken as systematic uncertainty in each centrality class. This leads to the uncertainty of 4.5% for the $\frac{3}{\Lambda}H$, independently of centralities, while the $\frac{3}{\Lambda}\bar{H}$ uncertainty slightly increases from 7 % to 7.5 % from the most central (0–10%) to the semi-central (30–50%) collisions.

The check on the assumption on the $\frac{3}{\Lambda}H$ cross-section value is performed in a similar way. In one case the correction is evaluated without rescaling the 3He cross-section, $\sigma_{\frac{3}{\Lambda}H} = 1 \cdot \sigma_{^3He}$, and in the other one the cross-section is increased by a factor 2, $\sigma_{\frac{3}{\Lambda}H} = 2 \cdot \sigma_{^3He}$. The raw yields are corrected with these two probabilities separately and the systematic uncertainty in each centrality class is assessed with semi-difference between the corrected yields. The result is a constant uncertainty of 4.5 % for the $\frac{3}{\Lambda}H$, while it goes from 7.3 % to 7.75 % for the $\frac{3}{\Lambda}\bar{H}$.

Another important check for the $(\frac{3}{\Lambda}\bar{H})\frac{3}{\Lambda}H$ analyses is on the efficiency calculation. As already explained, a weighted average is performed to obtain the efficiency \times acceptance values and the check is performed using different distribution as weights. In particular, the Blast-Wave from π -K-p production analysis [19], the Boltzmann and the m_T -exponential distributions from 3He analysis [6] are those used for the systematic uncertainty estimate. In addition, since the 3He Blast-Wave are not in the same centrality classes of this analysis and the $\frac{3}{\Lambda}H$ efficiency in the 30–50% used as weights the 3He Blast-Wave in 40–90 %, it is tried to calculate this efficiency with the 3He Blast-Wave in 10–40 % in the systematic studies. The $\frac{3}{\Lambda}H$ and $\frac{3}{\Lambda}\bar{H}$ yields are corrected with these efficiencies and the semidifference with respect to the reference values is assigned as systematic uncertainty to the yields extracted in the 30-50 % centrality class. The systematic uncertainties are 5.1% and 4.9% for $\frac{3}{\Lambda}H$ and $\frac{3}{\Lambda}\bar{H}$, respectively. A similar procedure has been done for the yields in 10-30%, since the weights for the efficiency are taken from the 3He Blast-Wave in 10–40 % and this led to a systematic uncertainty of 4.8% and 4.7% for $\frac{3}{\Lambda}H$ and $\frac{3}{\Lambda}\bar{H}$, respectively. The weighted average is calculated using these distributions and the raw yields are corrected with the obtained values. The rms of the corrected yields distribution is taken as systematic uncertainty and it decreases from 3 % to 1 % from the most central to the semi-central collisions.

The second check on the efficiency is performed in order to inquire into possible discrepancies in the evaluated reconstruction efficiency when changing the material budget estimation in the apparatus. This requires the usage of the MC productions introduced in Sec. 2.2, where the material budget has been increased and decreased by 4.5% respectively. The efficiency \times acceptance evaluated with these simulations are shown in Figure 16 and are compared with the results from MC simulation adopting the standard material budget. A trend with the material budget can be observed in each p_T interval, especially at low p_T . Reducing the material budget has the consequence of reducing the multiple scattering,

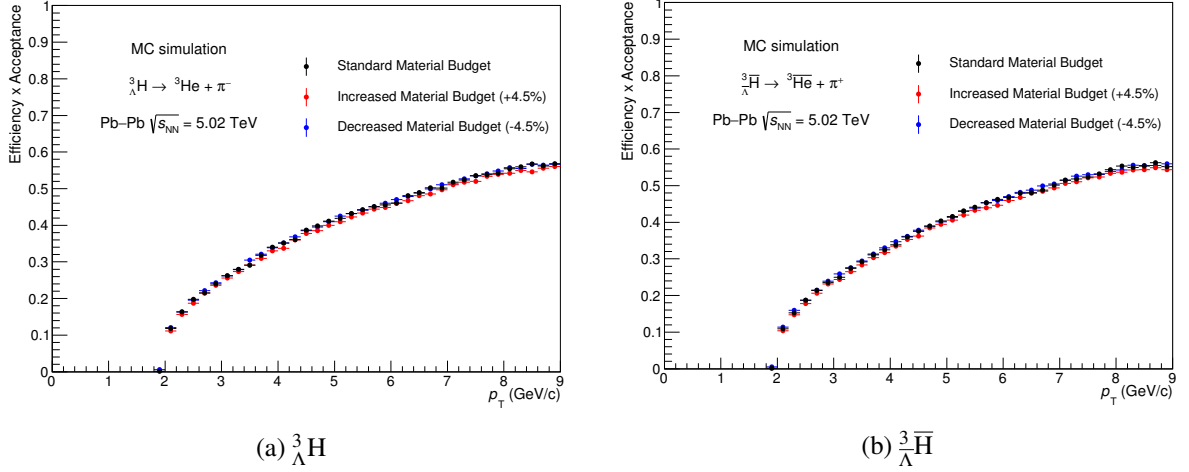


Fig. 16: Study of the effect of the material budget variation in the estimation of the efficiency \times acceptance for $\frac{3}{\Lambda}\text{H}$ (a) and $\frac{3}{\Lambda}\bar{\text{H}}$ (b).

thus increasing the tracks reconstruction efficiency (blue marker), while the decrease of the efficiency is related to the increased material budget. The variations in the efficiency \times acceptance induced by changing in the material budget distribution are supposed to follow a uniform distribution and, for this reason, the systematic uncertainty is estimated as:

$$\sigma_{MB}(p_T) = \frac{\varepsilon_{max}(p_T) - \varepsilon_{min}(p_T)}{\sqrt{12}} \quad (20)$$

where ε_{max} and ε_{min} are the maximum and minimum efficiency in each p_T interval. This uncertainty estimation lies between 0.5% and 0.8% in the analysed p_T range both for $\frac{3}{\Lambda}\text{H}$ and $\frac{3}{\Lambda}\bar{\text{H}}$ and it has been chosen to assign a systematic uncertainty due to the not perfect knowledge of the material budget of 1% in each p_T bin.

The variation of the selection criteria, like topological cuts and PID, applied to the candidates is the analysis approach used to investigate possible systematic effects related to the signal extraction. The variations of the topological and PID cuts with respect to the nominal ones (Table 7 and Table 13) are reported in Table 12 and in Table 13.

Candidate selection variations - systematics						
	Set 1	Set 2	Set 2	Set 4	Set 5	Set 6
$^3\text{He } p_T \text{ (GeV/c)} \geq$	1.7	1.8	1.6	1.9	1.9	1.8
$\text{DCA}_{tracks} \text{ (cm)} <$	0.6	0.5	0.6	0.5	0.7	0.5
$\cos(\theta_{pointing}) \geq$	0.997	0.992	0.995	0.992	0.997	0.997

Table 12: Set of cuts applied in the study of the systematics uncertainty related to the selection criteria of $\frac{3}{\Lambda}\text{H}$ and $\frac{3}{\Lambda}\bar{\text{H}}$ candidates.

For each of these selection variations the analysis is repeated *ab initio* for all centrality classes. Since the variation of the selection criteria modifies the sample of $(\frac{3}{\Lambda}\bar{H})_{\Lambda}^3\text{H}$ candidates, only the statistically significant variations of the final results have to be included in the systematic uncertainty. For this reason, a general prescription in ALICE is to compare the results obtained by changing the selection with the result obtained with the nominal selection and to include the cut and PID among the systematic uncertainties only if the difference is larger than 2σ . This method is usually called *Barlow criterion* from Roger Barlow's paper [18], where the variable used for the test $\Delta Y/\sigma_{\Delta}$ is introduced. Following

PID selection variations - systematics						
		Set 1	Set 2	Set 2	Set 4	Set 5
π	$ n\sigma_\pi \leq$	3	3	3	3	2
${}^3\text{He}$	$ n\sigma_{{}^3\text{He}} \leq$	3	3	2	2	3
	$n\sigma_{{}^3\text{H}} >$	3	6	6	3	0

Table 13: Set of $n\sigma$ cuts applied in the study of the systematics uncertainty related to the PID of ${}^3_\Lambda\text{H}$ and ${}^3_\Lambda\bar{\text{H}}$ daughters.

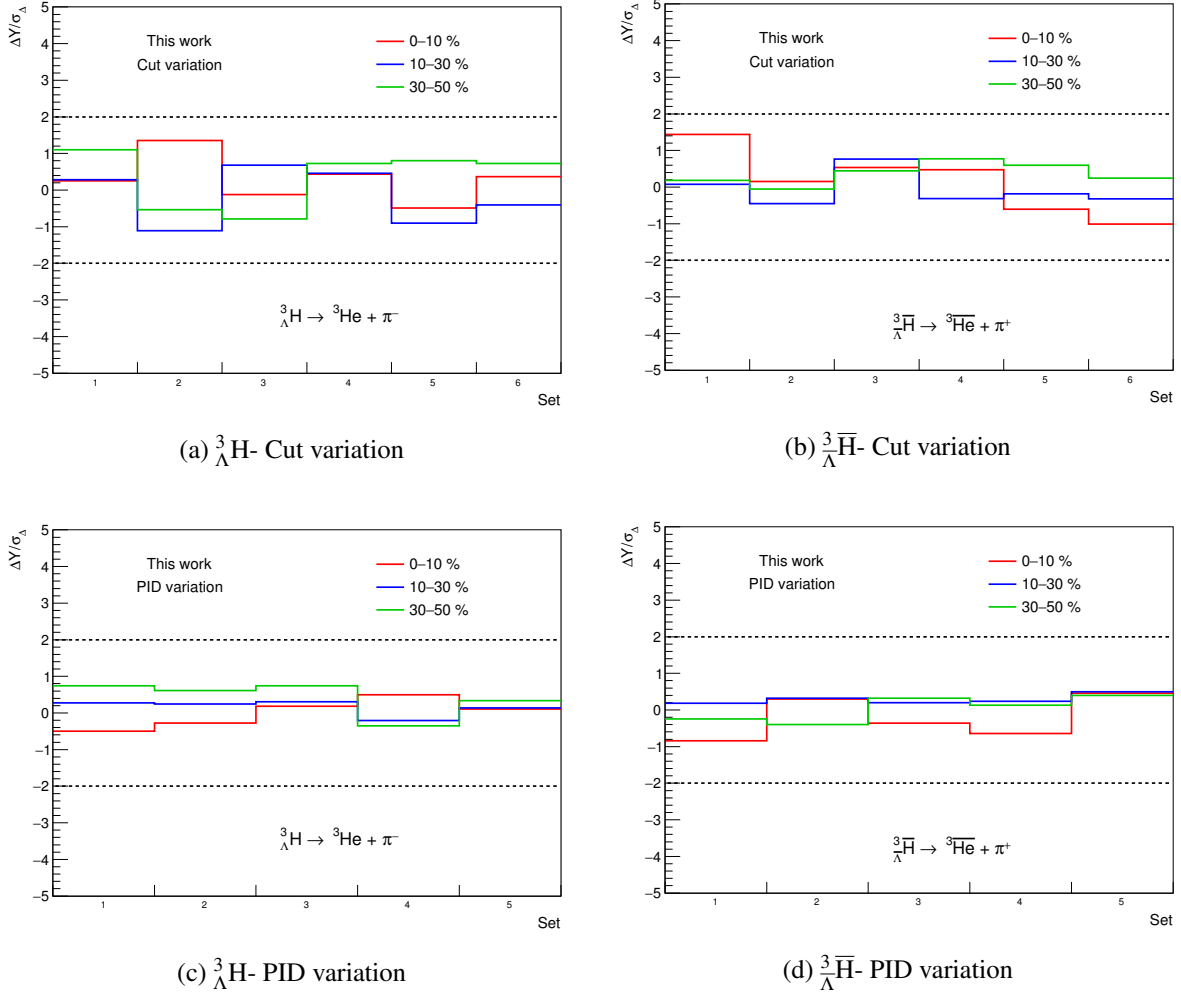


Fig. 17: Significance of the difference between the results obtained with nominal selections and those obtained with cuts (top) and PID (bottom) variations. The dashed line at ± 2 corresponds to the minimal threshold required in the *Barlow criterion* to include the variation in the systematic uncertainties.

this principle, the significance of the difference between the results is evaluated for all the variations both for matter and anti-matter and they are reported in Figure 17. All the results exhibit a difference which does not exceed the $\pm 2\sigma$ (dashed lines) and, for this reason, both the cut and PID selection criteria are not included among the sources of systematic uncertainties.

Considering the raw yield extraction, another check is performed on the function used for the background estimate. The analyses are repeated using two different functions for the background, the Landau and the third degree polynomial and, also in this case, the results are compared with those obtained with the

nominal function. Nevertheless, also this check is not included in the sources of systematic uncertainties because the Barlow test results are below the 2σ threshold.

The measured raw yields are obtained by selecting candidates $\frac{3}{\Lambda}\text{H}$ and $\frac{3}{\Lambda}\bar{H}$ in the p_T range 2-9 GeV/c. However the final production yields will be p_T integrated and the missing fraction is obtained from the integral of the Blast-Wave, that is the distribution used to describe the production spectra of light particles in heavy-ion collisions. In particular, the correction factor is the ratio between the integral of the distribution in the measured range (2-9 GeV/c) and the integral over the full p_T range. The raw yield is then divided for this value to include the missing fraction. Consequently, the distribution is the key element in this correction and the unknown p_T -shape in the unmeasured regions is a source of systematic uncertainties. The check is usually performed using different distributions to fit the p_T spectra, but in this case only the yields are available. For this reason the systematic uncertainty is taken from the analysis on the p_T production spectra of $(\frac{3}{\Lambda}\bar{H})_{\Lambda}^3\text{H}$, which will be described in Sec. 6. In particular details on the evaluation of this source of systematic will be given in Sec. 6.4. The value of this uncertainty is 6.7 % for $\frac{3}{\Lambda}\text{H}$ and 6.5 % for $\frac{3}{\Lambda}\bar{H}$ in all centrality classes.

Finally, the last systematic effect is common to all the analyses in ALICE and is related to the tracking efficiency. Indeed it is not known to which extent the simulation reproduces the reality and the efficiency calculation can be a source of systematic uncertainty. This effect has been measured in the analysis of transverse momentum spectra of primary charged particles [20] in Pb–Pb collisions and the result is an uncertainty of 3.5 % on each single track. Since in the reconstruction of the $(\frac{3}{\Lambda}\bar{H})_{\Lambda}^3\text{H}$ two daughters tracks are used and in order to be conservative, the systematic uncertainty is assessed at 7 %.

In Table 14 the uncertainties, related to systematic effects previously described, are reported for $\frac{3}{\Lambda}\text{H}$ (left) and $\frac{3}{\Lambda}\bar{H}$ (right) in all centrality classes. The total systematic uncertainties assigned to the final corrected yield is obtained with a sum in quadrature of the single sources, assuming all of them as uncorrelated.

Source	Systematic uncertainties					
	$\frac{3}{\Lambda}\text{H}$			$\frac{3}{\Lambda}\bar{H}$		
	0–10%	10–30%	30–50%	0–10%	10–30%	30–50%
Cross-section	4.48%	4.48%	4.5%	7%	7.28%	7.5%
Average absorption correction	4.49%	4.5%	4.51%	7.3%	7.5%	7.75%
Efficiency weights	3.1%	2.7%	1.6%	3.2%	2.8%	1.6%
Centrality bin ^3He BW weighted efficiency	-	4.8%	5.1 %	-	4.7%	4.9 %
Material budget		1%			1%	
Unknown p_T -shape		6.7%			6.5%	
Single track efficiency		7%			7%	
Total	12%	12.9%	12.8%	14.3%	15.2%	15.3%

Table 14: Summary of the systematic uncertainties in the production yields analysis. The total uncertainty assigned in each centrality class is the sum in quadrature of the single sources.

The aforementioned corrections and the systematic uncertainties will be used in the calculation of the production yields of $\frac{3}{\Lambda}\text{H}$ and $\frac{3}{\Lambda}\bar{H}$ in the 2 body decay channel in three centrality classes.

5.5 Corrected yields

The $(\frac{3}{\Lambda}\bar{H})_{\Lambda}^3\text{H}$ dN/dy are obtained with the following formula:

$$\frac{dN}{dy} = \frac{1}{N_{\text{ev}}} \frac{f_{\text{missing}}}{\epsilon \cdot f_{\text{absorption}}} \frac{dN_{\text{raw}}}{dy} \quad (21)$$

where N_{ev} is the total number of events analysed in each centrality class, ε is the acceptance \times efficiency correction, $f_{\text{absorption}}$ is the absorption correction and f_{missing} is the estimated fraction of the total yields in the unmeasured p_{T} regions, since the raw yields are measured in the 2-9 GeV/c interval. The results are reported in Table 15

Yields vs centrality			
	$dN/dy \times \text{B.R.} \times 10^{-5}$		
	${}^3_{\Lambda}\text{H}$	${}^3_{\Lambda}\bar{\text{H}}$	
0–10%	$3.37 \pm 0.77(\text{stat.}) \pm 0.40(\text{syst.})$	$3.38 \pm 0.70(\text{stat.}) \pm 0.48(\text{syst.})$	
10–30%	$1.28 \pm 0.33(\text{stat.}) \pm 0.17(\text{syst.})$	$1.30 \pm 0.36(\text{stat.}) \pm 0.2(\text{syst.})$	
30–50%	$0.77 \pm 0.23(\text{stat.}) \pm 0.1(\text{syst.})$	$0.77 \pm 0.25(\text{stat.}) \pm 0.12(\text{syst.})$	

Table 15: Integrated yields per rapidity unit dN/dy times the B.R. of the 2 body decay channel, for the ${}^3_{\Lambda}\text{H}$ and ${}^3_{\Lambda}\bar{\text{H}}$ in the centrality classes analysed of the Pb–Pb collisions at $\sqrt{s_{\text{NN}}} = 5.02$ TeV.

6 p_{T} production spectra

The second part of the production analysis concerns the measurement of the p_{T} spectrum of ${}^3_{\Lambda}\text{H}$ and ${}^3_{\Lambda}\bar{\text{H}}$. Due to the available statistics in semi-central events, the study of the production p_{T} spectra is performed in the 10–40% centrality class. The steps followed to obtain the final result are the same previously described for the measurement of the corrected yields and, for this reason, only the outcomes from each steps are presented in the following.

6.1 Raw yields extraction vs p_{T}

The raw yields are measured as a function of the p_{T} and they are obtained from the invariant mass distributions of the ${}^3_{\Lambda}\text{H}$ and ${}^3_{\Lambda}\bar{\text{H}}$. In particular, the p_{T} intervals selected for this analysis are 2-3, 3-4, 4-5 and 5-9 GeV/c. The candidates $({}^3_{\Lambda}\bar{\text{H}}){}^3_{\Lambda}\text{H}$ are selected applying the selection criteria previously described and reported in Table 16. In this second part of the analysis the candidates are split in narrow p_{T} intervals and this means a lower signal in each of them if compared with the p_{T} integrated analysis (Sec 5.1). Thus, in order to increase the statistics, especially in the first p_{T} interval, the selection on the minimum ${}^3\text{He}$ p_{T} is of 1.6 GeV/c. On the other hand, the cut on the $\text{DCA}_{\text{tracks}}$ and on the $\cos(\theta_{\text{pointing}})$ are restricted to 0.6 and 0.997 respectively to further reduce the combinatorial background.

Candidate selections		
	${}^3_{\Lambda}\text{H}$	${}^3_{\Lambda}\bar{\text{H}}$
π p_{T} (GeV/c)	0.2-1.2	0.2-1.2
${}^3\text{He}$ p_{T} (GeV/c)	≥ 1.6	≥ 1.6
$\text{DCA}_{\text{tracks}}$ (cm)	< 0.6	< 0.6
ct (cm)	> 2	> 2
$\cos(\theta_{\text{pointing}})$	≥ 0.997	≥ 0.997
$ y $	≤ 0.5	≤ 0.5

Table 16: Set of cuts applied for the selection of ${}^3_{\Lambda}\text{H}$ and ${}^3_{\Lambda}\bar{\text{H}}$ candidates in different p_{T} intervals in the 10–40% centrality class.

The invariant mass distribution of the candidates ${}^3_{\Lambda}\text{H}$ and ${}^3_{\Lambda}\bar{\text{H}}$ in the four p_{T} intervals are shown in Figure 18 and 19, respectively. The distribution of the ${}^3_{\Lambda}\text{H}$ in the 2-3 GeV/c shows a higher combinatorial background if compared to the others. It is mainly due to the contamination of secondary ${}^3\text{He}$ produced by knock-out with the material which dominates the low p_{T} region.

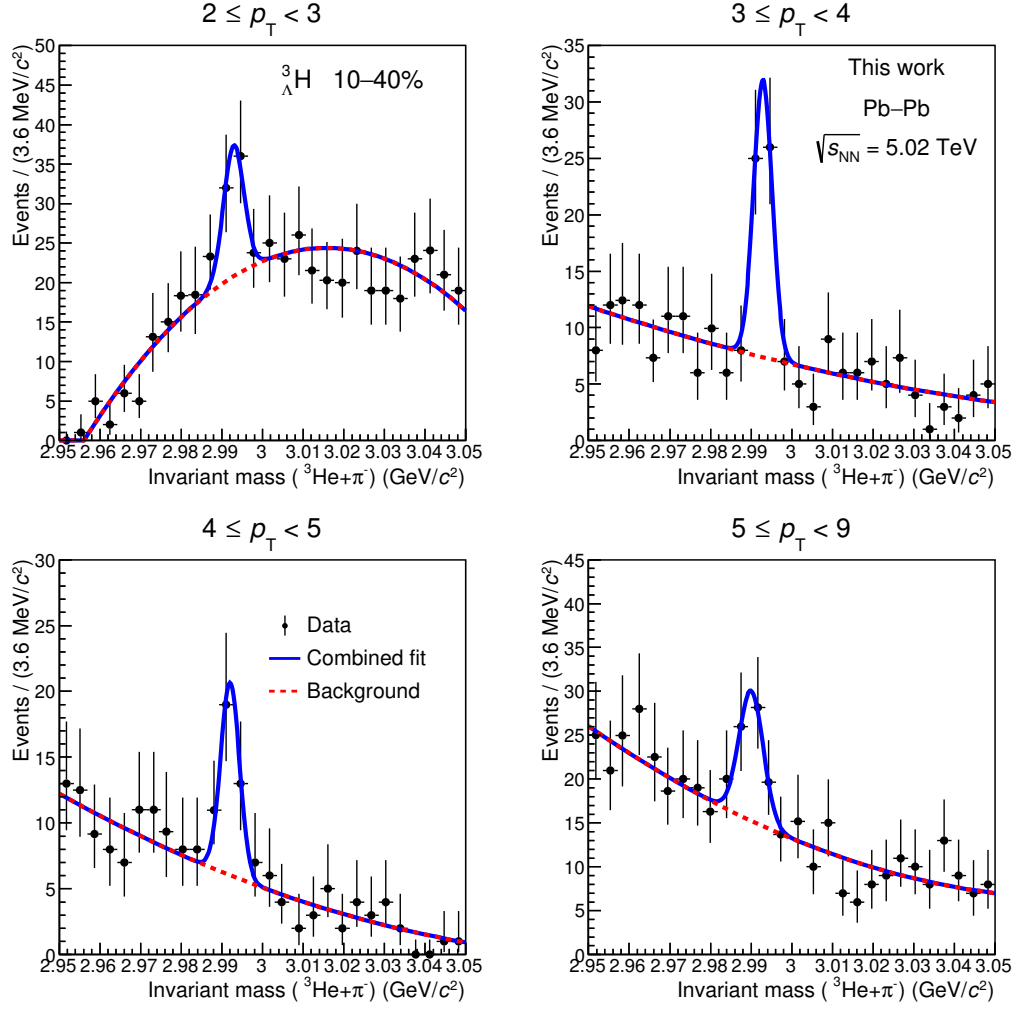


Fig. 18: ${}^3_{\Lambda}\text{H}$ invariant mass distributions in the four p_T intervals. The blue curve is the fitting function and the red dashed curve is the background component.

The raw yield extraction is performed with a fit to the distribution using a combined function (blue curve), that is the sum of a Gaussian for the signal and a second degree polynomial (dashed red curve) for the background. As already introduced in Eq. 12, the normalization is kept into account with N_{sig} and N_{bkg} , which represent the raw signal and background counts.

The fit is performed separately for the ${}^3_{\Lambda}\text{H}$ and the ${}^3_{\Lambda}\bar{\text{H}}$ for the first three p_T bins (2–3, 3–4, 4–5 GeV/c). In the last p_T interval, instead, the raw yield extraction is performed in two steps because of the low statistics. A first fit is performed to the invariant mass distribution obtained with the sum of ${}^3_{\Lambda}\text{H}$ and ${}^3_{\Lambda}\bar{\text{H}}$ and the σ from the fit result is used in the second step. Indeed, the fit for the raw yield extraction is performed separately for matter and anti-matter, having fixed the width of the Gaussian to the σ previously found.

The mean values (μ) of the Gaussian obtained from the fits are compared to the experimental mass value measured by ALICE [5] and STAR [13], as shown in Figure 20a and Figure 20b. The results of the fit as well as the S/B ratio and the significance of the extracted raw yields are reported in Table 17 for the ${}^3_{\Lambda}\text{H}$ and in Table 18 for the ${}^3_{\Lambda}\bar{\text{H}}$ for the different p_T intervals. The raw yields (S) and the background counts (B) are obtained from the integral, of the respective components of the fitting function, in the invariant mass range $\mu \pm 3\sigma$.

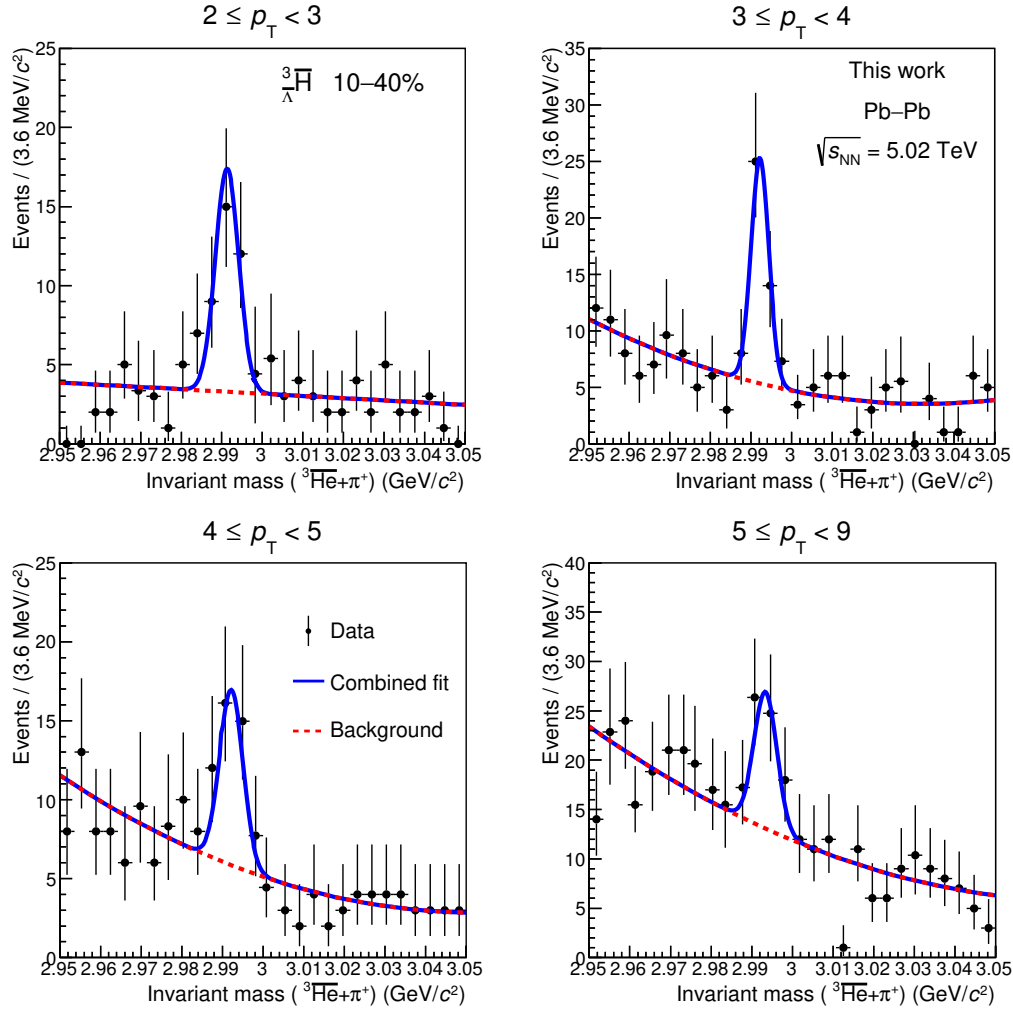


Fig. 19: $\bar{\Lambda}^3\text{He}$ invariant mass distributions in the four p_T intervals. The blue curve is the fitting function and the red dashed curve is the background component.

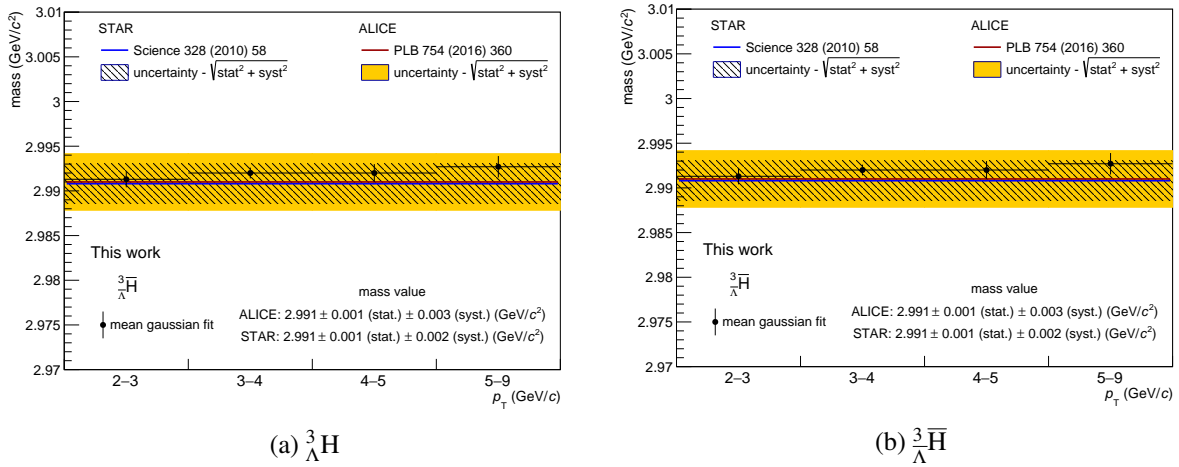


Fig. 20: Mean values with their uncertainties obtained from the fit to the $\bar{\Lambda}^3\text{He}$ (a) and $\bar{\Lambda}^3\text{He}$ (b) invariant mass distributions compared with the experimental mass value measured by STAR [13] and ALICE [5].

p_{T} (GeV/ c)	$\frac{3}{\Lambda}\text{H}$			
	2-3	3-4	4-5	5-9
mean (GeV/ c^2)	2.9929 ± 0.0008	2.9928 ± 0.0005	2.9921 ± 0.0007	2.9902 ± 0.0008
width (GeV/ c^2)	0.0025 ± 0.0003	0.0023 ± 0.0004	0.0023 ± 0.0003	0.0029 ± 0.0008
χ^2/NDF	1.74	2.00	1.08	1.09
S/B	0.51	1.80	1.29	0.44
Significance (3σ)	3.11	4.95	3.54	2.69
Raw yield	27 ± 7	33 ± 7	24 ± 6	25 ± 8

Table 17: Results of the fit to the $\frac{3}{\Lambda}\text{H}$ invariant mass distributions in the four p_{T} intervals. Raw yields are obtained as the integral of the signal function in $\pm 3\sigma$ with respect to the mean value.

p_{T} (GeV/ c)	$\frac{3}{\Lambda}\bar{\text{H}}$			
	2-3	3-4	4-5	5-9
mean (GeV/ c^2)	2.9913 ± 0.0009	2.9922 ± 0.0006	2.9922 ± 0.0010	2.9931 ± 0.0015
width (GeV/ c^2)	0.0028 ± 0.0006	0.0023 ± 0.0006	0.0028 ± 0.0005	0.0029 ± 0.0008
χ^2/NDF	1.87	1.89	1.03	2.86
S/B	1.94	1.73	0.99	0.44
Significance (3σ)	4.26	4.24	3.31	2.45
Raw yield	21 ± 6	26 ± 6	23 ± 6	26 ± 8

Table 18: Results of the fit to the $\frac{3}{\Lambda}\bar{\text{H}}$ invariant mass distributions in the four p_{T} intervals. Raw yields are obtained as the integral of the signal function in $\pm 3\sigma$ with respect to the mean value.

6.2 Efficiency correction

The efficiency \times acceptance distribution is evaluated, as previously described in Sec. 5.2, with the ratio of the number of reconstructed $(\bar{\Lambda}^3\bar{H})_{\Lambda}^3H$ which satisfies the selections of Table 16 and the number of generated $(\bar{\Lambda}^3\bar{H})_{\Lambda}^3H$ in the rapidity range $|y| < 0.5$. The distributions are reported with open markers in Figure 21a and 21b for the Λ^3H and $\bar{\Lambda}^3\bar{H}$ respectively.

The efficiency \times acceptance in the p_T intervals used in the analysis is obtained with a weighted average of the distributions in the same p_T ranges. The weights are taken from the Blast-Wave distribution obtained from the ${}^3\text{He}$ production analysis and the result of the weighted average are reported as histogram in Figure 21a and 21b. In addition the values of the efficiency in the p_T intervals and for the Λ^3H and the $\bar{\Lambda}^3\bar{H}$ are reported in Table 19.

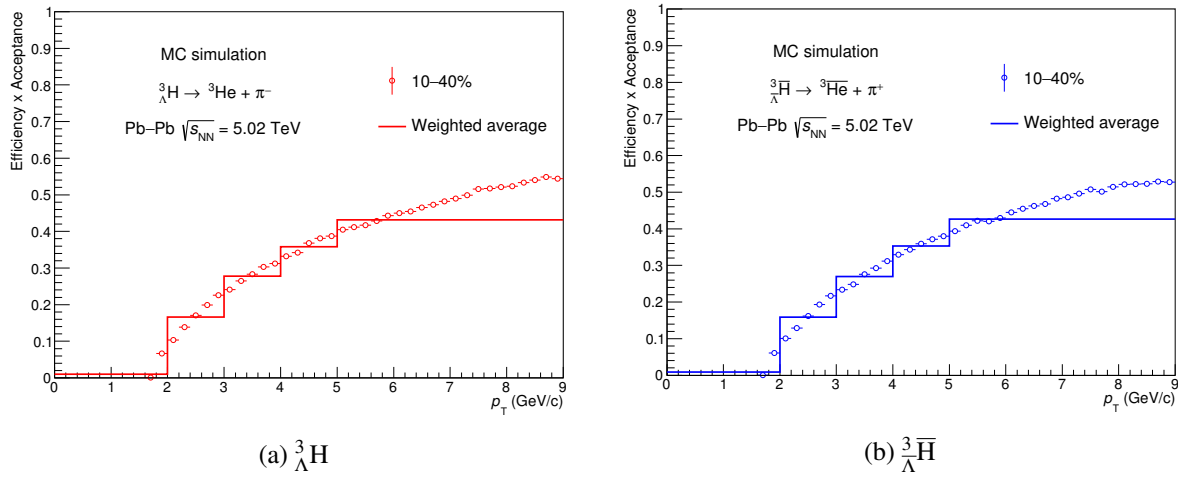


Fig. 21: Efficiency \times acceptance distribution (open markers) for the Λ^3H (a) and the $\bar{\Lambda}^3\bar{H}$ (b). The line represents the efficiency in the p_T intervals of this analysis obtained with a weighted average of the distribution.

Efficiency \times Acceptance				
p_T (GeV/c)	2-3	3-4	4-5	5-9
Λ^3H	16.6%	27.8%	35.8%	43.1%
$\bar{\Lambda}^3\bar{H}$	15.9%	26.9%	35.3%	42.6%

Table 19: Efficiency \times acceptance for the Λ^3H and the $\bar{\Lambda}^3\bar{H}$ obtained with a weighted average in the four analyzed p_T intervals.

6.3 Absorption correction

The evaluation of the absorption correction is the procedure described in detail in Sec. 5.3. In particular, the distribution of the probability to observe p_{Observe} the Λ^3H (Figure 15a) and the $\bar{\Lambda}^3\bar{H}$ (Figure 15b) are used to evaluate the absorption probability in the p_T intervals of this analysis. It is important to remember that these distributions are evaluated as a function of the $(\bar{p})p$ p_T . Thus, in order to find the corresponding p_T interval in these distributions one has to keep in mind that $p_T = p_{\Lambda^3H}^{\Lambda}/3$ (e.g. 2-3 \rightarrow 0.66-1 GeV/c).

The probability to observe the $(\bar{\Lambda}^3\bar{H})_{\Lambda}^3H$ in the four p_T ranges is obtained as weighted average of the distributions, using the ${}^3\text{He}$ Blast-Wave distribution as weight and the results are shown in Figure 22. The red line is the probability to observe the Λ^3H , while the blue line is the same probability for the $\bar{\Lambda}^3\bar{H}$. The rise of the distribution of the $\bar{\Lambda}^3\bar{H}$ corresponds to a higher absorption in the low p_T region, while this

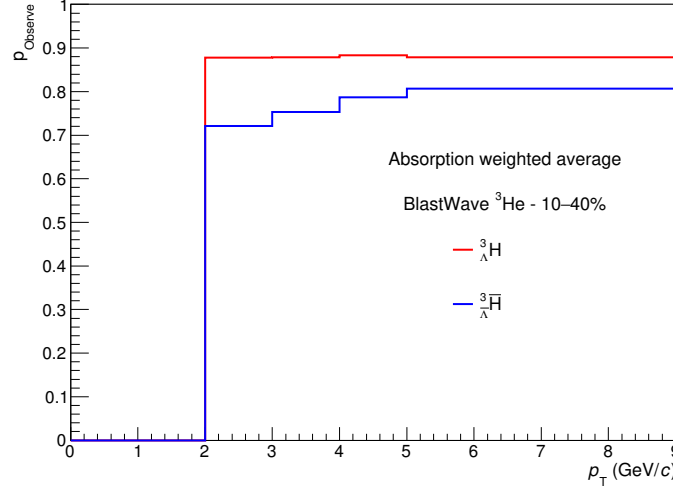


Fig. 22: Distribution of the probability to observe the $\frac{3}{\Lambda}H$ (red) and the $\frac{3}{\Lambda}\bar{H}$ (blue). The values in the p_T intervals of this analysis are obtained with a weighted average.

Absorption correction				
p_T (GeV/c)	2-3	3-4	4-5	5-9
$\frac{3}{\Lambda}H$	87.8%	87.8%	88.3%	87.8%
$\frac{3}{\Lambda}\bar{H}$	72.3%	75.3%	78.7%	80.6%

Table 20: Probability to observe the $\frac{3}{\Lambda}H$ and the $\frac{3}{\Lambda}\bar{H}$ obtained with a weighted average in the four p_T intervals.

effect is constant for the $\frac{3}{\Lambda}H$ as a function of p_T . In addition the values of the absorption correction factor are reported in Table 20.

6.4 Systematics uncertainties

The sources of the systematic uncertainty that have been checked in the analysis of the p_T production spectra analysis are the same previously introduced and described in detail for the production yields as a function of the collision centrality (see Sec. 5.4). The main difference is that in this case the systematics are assessed on the yields in the different p_T intervals, while previously they were evaluated directly on the integrated yield. The results of the checks on the different contribution together with the total systematic uncertainty are shown in Figure 23a and 23b.

The contribution of the absorption correction in the systematic uncertainty is related to the usage of an average correction and to the scale factor applied in the $\sigma_{\frac{3}{\Lambda}H}$. The checks give a flat uncertainty at ~ 4.5 % for the $\frac{3}{\Lambda}H$ as a function of p_T , while for the $\frac{3}{\Lambda}\bar{H}$ it decreases from ~ 8.3 % at low p_T to ~ 6 % at high p_T for both sources. In Figure 23a the contribution of the cross section (red line) and of the absorption (blue line) are overlapped because of they are similar, thus only the blue line is visible.

The systematic uncertainties on the efficiency calculation are evaluated firstly by changing the distributions used as weight in the average and this gives an uncertainty from 0.4 % to 2.6 % both for the $\frac{3}{\Lambda}H$ and the $\frac{3}{\Lambda}\bar{H}$. In particular, as shown in Figure 23, the higher uncertainty is in the 5-9 p_T interval and this is due to the weighted average computation in that range. Indeed, the $(\frac{3}{\Lambda}\bar{H})\frac{3}{\Lambda}H$ efficiency distribution is between 0.4 and 0.5 from 5 to 9 GeV/c, while the weights distribution have large variation from one p_T -distribution to another. Thus, the effect of using different functions as weights is a larger systematic uncertainty in that p_T interval.

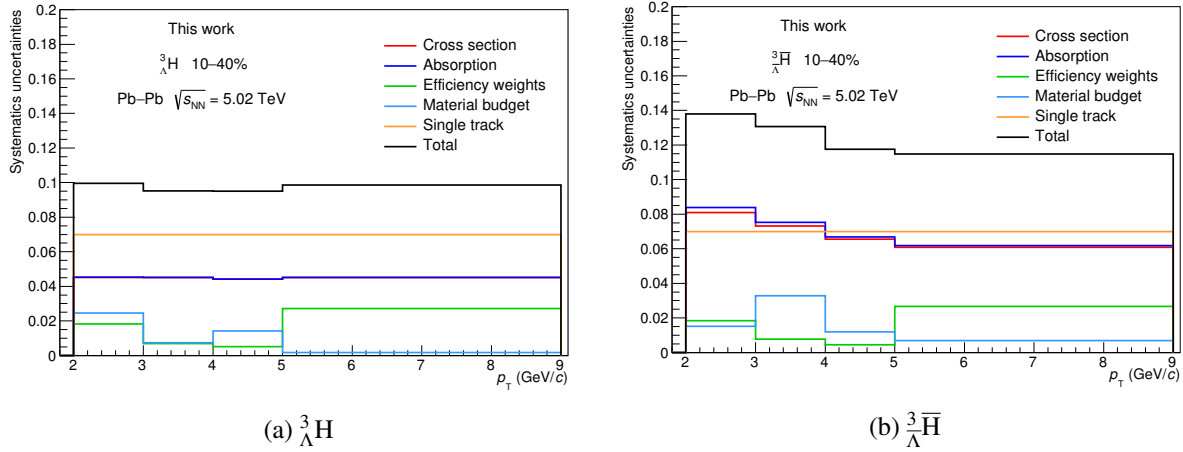


Fig. 23: Systematic uncertainties for the ${}^3\Lambda H$ (a) and the ${}^3\Lambda \bar{H}$ (b) as a function of p_T . The colored lines are the systematic uncertainties of the single sources, while the black line is the total uncertainty in each p_T interval.

The effect of the uncertainty on the material budget used in the simulation is studied, as already described, using two MC productions with the material budget varied of $\pm 4.5\%$ with respect to the nominal one. Following what previously done and using Eq.20 the systematic uncertainty is 1 % for both particle and anti-particle in all the p_T ranges.

The criteria applied for the candidates selection are another source inspected in this analysis. The different set of cuts and PID requirements, previously introduced and reported in Tables 12 and 13, are tested and the Barlow criterion is also used to select variations with a significance larger than 2σ if compared with the value obtained with the nominal cuts. In this case the variable introduced in the Barlow criterion $\Delta Y/\sigma_\Delta$ is calculated for the yield variation in each single p_T interval. Figures 24a and 24b show the trend of the Barlow variable for the different set of cuts and for the different p_T intervals, represented with four different colored lines. The same distributions are also studied for the variation on the PID selections and they are reported in Figure 24c and 24d. The result shows that the variations induced by changing the cuts are within the threshold of ± 2 used in the application of the Barlow criterion. Thus these systematic uncertainties are not included in the total systematic uncertainty. Moreover, the same result is obtained also for the test on the fitting function used for the yield extraction. Indeed, the distribution used for the background component are replaced with a Landau and a third degree polynomial and in both cases the variations are not significantly large to be included in the systematic uncertainties.

The effect related to the single track efficiency has already been introduced in Sec 5.4 and, as previously done, the uncertainty is assessed as twice the single tracking efficiency systematic uncertainty (3.5% from [20]), which means 7 % for all p_T intervals.

Finally, the unknown p_T -shape is an important source of uncertainty. Indeed, the p_T spectra are measured in a limited region from 2 to 9 GeV/c and the integrated yield is obtained with a fit to the measured spectra. As a consequence, the choice of the fit function plays a crucial role. As it will be shown in Sec. 7, where the results are presented and compared with the theoretical models, the Blast-Wave distribution is used to describe the p_T spectra of particles produced in heavy-ion collisions. To check the effect of this choice and to evaluate a systematic uncertainty, the fit is repeated using different distributions: the Blast-Wave distribution with parameters extracted from π, K, p analysis, the Boltzmann function, the mT-exponential, the simple exponential, the Bose-Einstein and the Fermi-Dirac distributions. When using the Blast-Wave as a fit function the parameters are fixed to those obtained in previous analysis and the reason is that the number of yields in the p_T spectra is lower than the number of parameters. For the other functions, instead, a fit with free parameters is performed. However, in order to be more conservative

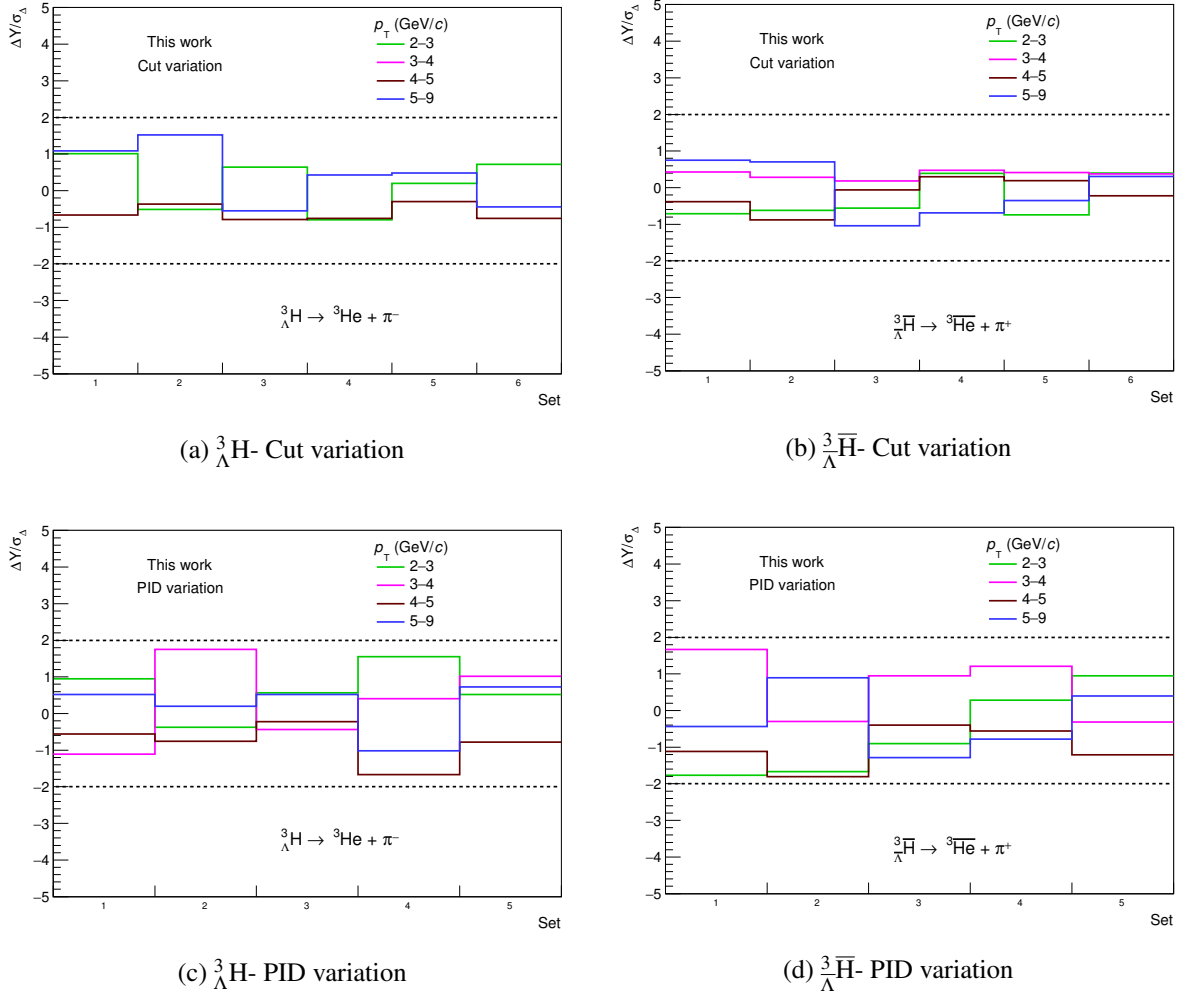


Fig. 24: Significance of the difference between the results obtained with nominal selections and those obtained with cuts (top) and PID (bottom) variations. The dashed line at ± 2 corresponds to the minimal threshold required in the *Barlow criterion* to include the variation in the systematic uncertainties.

for this estimation, the uncertainty is assessed taking the semi-difference of the maximum and minimum values of the integrals of the distributions in the unmeasured p_T regions. This lead to a 6.7% for the ^3H and a 6.5% $\bar{^3\text{H}}$. These uncertainties are directly obtained on the integrated yield, so they will be added only to the total systematic on the integrated yield. Moreover, as previously anticipated, these uncertainties are also assigned to the production yields analysis described in Sec. 5.4.

The values of the systematic uncertainties in each p_T interval are reported in Table 21 and the total systematic uncertainty is the sum in quadrature of the single sources. Only the systematic due to the unknown p_T -shape is excluded in the total uncertainty of the single p_T bin, as it is measured and assigned directly to the integrated yield.

Systematic uncertainties								
Source	${}^3_{\Lambda}\text{H}$				${}^3_{\Lambda}\bar{\text{H}}$			
p_{T} GeV/c	2–3	3–4	4–5	5–9	2–3	3–4	4–5	5–9
Cross-section	4.50%	4.51%	4.41%	4.50%	8.1%	7.3%	6.5%	6.1%
Average absorption correction	4.52%	4.52%	4.42%	4.52%	8.3%	7.5%	6.7%	6.2%
Efficiency weights	1.83%	0.7%	0.5%	2.7%	1.83%	0.8%	0.4%	2.6%
Material budget			1%				1%	
Single track efficiency			7%				7%	
Unknown p_{T} -shape (on integrated yield)			6.7%				6.5%	
Total	9.96%	9.52%	9.5%	9.85%	13.8%	13.1%	11.7%	11.4%

Table 21: Summary of the systematic uncertainties in the production yields analysis. The total uncertainty assigned in each p_{T} interval, except the Unknown p_{T} -shape, is the sum in quadrature of the single sources.

7 Results

7.1 p_{T} spectra

By combining the information of the signal extraction and the corrections described in Sec. 6, the production spectra of the $({}^3_{\Lambda}\bar{\text{H}}){}^3_{\Lambda}\text{H}$ in 10–40% are evaluated as:

$$\frac{1}{N_{\text{ev}}} \frac{d^2N}{dp_{\text{T}}dy} = \frac{1}{N_{\text{ev}}} \frac{1}{\varepsilon \cdot f_{\text{absorption}}} \frac{dN_{\text{raw}}}{dp_{\text{T}}} \quad (22)$$

where N_{ev} is the total number of analysed events, ε is the efficiency \times acceptance correction, $f_{\text{absorption}}$ is the absorption correction and N_{raw} is the raw yield in each p_{T} interval. Figures 25 and 26 show the corrected p_{T} spectrum for the ${}^3_{\Lambda}\text{H}$ and ${}^3_{\Lambda}\bar{\text{H}}$, respectively, measured for the first time in semi-central collisions (10–40%). The corrected yields are drawn at the corresponding p_{T} value obtained from the evaluation of the mean p_{T} assuming a Blast-Wave [21] distribution of the transverse momentum in each interval. The reason for this approach is related to the fact that the p_{T} intervals of the spectrum are not small enough to assume a flat p_{T} distribution and the Blast-Wave distribution is assumed, since it well describes the spectra of lighter particles [23] and nuclei [22] in heavy ion collisions.

In order to measure the total yield per rapidity unit dN/dy in the 10–40% centrality class, the ${}^3_{\Lambda}\text{H}$ and ${}^3_{\Lambda}\bar{\text{H}}$ spectra were fitted with the Blast-Wave function, represented with a dotted line in Figure 25 and 26. This function describes the measured spectra assuming a thermal production of particles from an expanding source:

$$\frac{1}{p_{\text{T}}} \frac{dN}{dp_{\text{T}}} \propto \int_0^R r dr m_{\text{T}} I_0 \left(\frac{p_{\text{T}} \sinh \rho}{T_{\text{kin}}} \right) K_1 \left(\frac{m_{\text{T}} \cosh \rho}{T_{\text{kin}}} \right) \quad (23)$$

where m_{T} is the transverse mass defined as $m_{\text{T}} = \sqrt{m^2 + p_{\text{T}}^2}$, I_0 and K_1 are the modified Bessel functions, r is the distance from the centre of the expanding system, R is the limiting radius of the system expansion, T_{kin} is the temperature of the kinetic freeze-out and ρ is the velocity profile. The velocity profile can be expressed in terms of the transverse expansion velocity at the system surface, β_{S} , and an exponent n :

$$\rho = \tanh^{-1} \left(\left(\frac{r}{R} \right)^n \beta_{\text{S}} \right) \quad (24)$$

In addition, the distribution introduced in Eq. 23 has to be multiplied for the parameter *norm* which takes into account the normalization of the distribution and corresponds to the integral of the Blast-Wave over the full p_{T} range. However, since the number of parameters of the Blast-Wave function is larger than the measured yield values, it has been chosen to fix them to those of the ${}^3\text{He}$ distribution [6], leaving only the

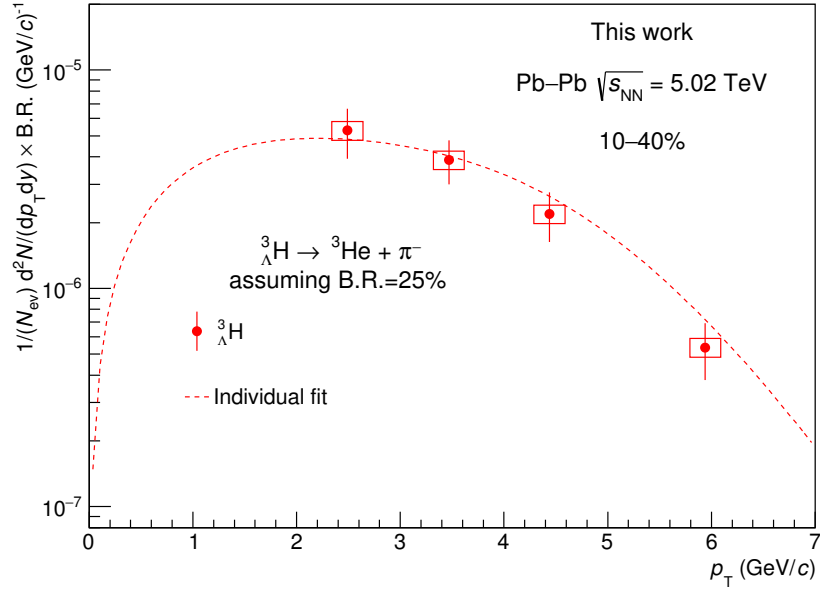


Fig. 25: ${}^3\text{H}$ transverse momentum spectrum measured in the centrality class 10–40% and in the rapidity range $|y| < 0.5$. The dotted line is the Blast-Wave function with fixed ${}^3\text{He}$ parameters.

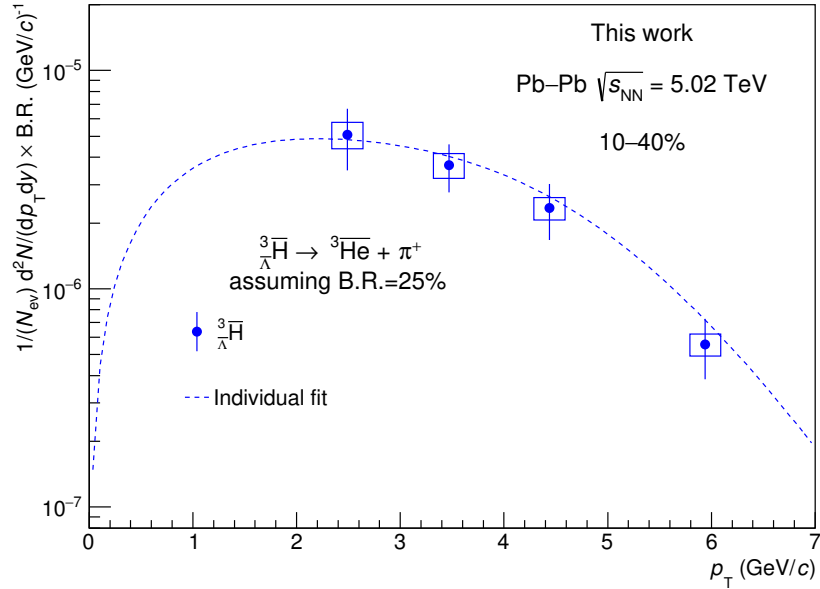


Fig. 26: ${}^3\bar{\text{H}}$ transverse momentum spectrum measured in the centrality class 10–40% and in the rapidity range $|y| < 0.5$. The dotted line is the Blast-Wave function with fixed ${}^3\text{He}$ parameters.

normalization as free parameters. The two individual fits well describe the measured p_T spectra of ${}^3\text{H}$ ($\chi^2/\text{NDF} = 0.588$) and ${}^3\bar{\text{H}}$ ($\chi^2/\text{NDF} = 0.498$) and this suggests that also their emission from the medium created in the collision is driven by the radial flow, which indicates the presence of a medium. Indeed, the Blast-Wave distribution is derived in a phenomenological model that describes the hadron spectra from heavy ion collisions in terms of a few collective variables, in particular temperature, longitudinal, and transverse (or radial) flow. The latter one is a collective motion that, in heavy ion collision, is interpreted as related to the pressure gradients of a deconfined medium.

In order to give a quantitative estimate of the radial flow effect from the $(\frac{3}{\Lambda}\bar{\text{H}})\frac{3}{\Lambda}\text{H}$ production it is necessary to perform a fit to the production spectra using the Blast-Wave with all the parameters free and not constrained as in this case. This will be possible by analysing the data sample of Pb–Pb collisions that will be collected at the end of 2018, where an increase by a factor 2 of the statistics, especially for the central collisions, is expected and this will lead to a production spectra with measured yields in narrower p_{T} interval.

The total yields per rapidity unit in the 10–40% centrality class are obtained from the integral of the aforementioned individual fit function over the full p_{T} range and the results are reported in Table 22.

Yields 10–40%		
	$dN/dy \times \text{B.R.} \times 10^{-5}$	$\langle dN_{ch}/d\eta \rangle$
$\frac{3}{\Lambda}\text{H}$	$1.24 \pm 0.21(\text{stat.}) \pm 0.12(\text{syst.})$	826 ± 22
$\frac{3}{\Lambda}\bar{\text{H}}$	$1.23 \pm 0.20(\text{stat.}) \pm 0.16(\text{syst.})$	826 ± 22

Table 22: Integrated yields per rapidity unit dN/dy times the Branching Ratio (B.R.) of the 2 body decay channel, for the $\frac{3}{\Lambda}\text{H}$ and $\frac{3}{\Lambda}\bar{\text{H}}$ in the centrality class 10–40% of the Pb–Pb collisions at $\sqrt{s_{\text{NN}}} = 5.02$ TeV. For the analysed centrality class the average $\langle dN_{ch}/d\eta \rangle$ is reported.

7.2 dN/dy as a function of centrality

Similarly, combining the information described in Sec. 5, the corrected total yields in the three centrality classes 0–10%, 10–30%, 30–50% are evaluated as:

$$\frac{dN}{dy} = \frac{1}{N_{\text{ev}}} \frac{f_{\text{missing}}}{\varepsilon \cdot f_{\text{absorption}}} \frac{dN_{\text{raw}}}{dy} \quad (25)$$

where N_{ev} is the total number of analysed events, ε is the acceptance \times efficiency correction, $f_{\text{absorption}}$ is the absorption correction and f_{missing} is the estimated fraction of the total yields in the unmeasured p_{T} regions, since the raw yields are measured in the 2–9 GeV/ c interval (see Sec. 5). The estimate of the yield in the unmeasured regions is done using the ${}^3\text{He}$ Blast-Wave function previously introduced [21] and the missing fraction is evaluated as the ratio of the integral in the unmeasured regions to the total integral. The total corrected yields per rapidity unit for the three centrality classes are reported in Table 23.

Yields vs centrality			
	$dN/dy \times \text{B.R.} \times 10^{-5}$		
	$\frac{3}{\Lambda}\text{H}$	$\frac{3}{\Lambda}\bar{\text{H}}$	$\langle dN_{ch}/d\eta \rangle$
0–10%	$3.37 \pm 0.77(\text{stat.}) \pm 0.40(\text{syst.})$	$3.38 \pm 0.70(\text{stat.}) \pm 0.48(\text{syst.})$	1756 ± 52
10–30%	$1.28 \pm 0.33(\text{stat.}) \pm 0.17(\text{syst.})$	$1.30 \pm 0.36(\text{stat.}) \pm 0.2(\text{syst.})$	983 ± 25
30–50%	$0.77 \pm 0.23(\text{stat.}) \pm 0.1(\text{syst.})$	$0.77 \pm 0.25(\text{stat.}) \pm 0.12(\text{syst.})$	415 ± 14

Table 23: Integrated yields per rapidity unit dN/dy times the B.R. of the 2 body decay channel, for the $\frac{3}{\Lambda}\text{H}$ and $\frac{3}{\Lambda}\bar{\text{H}}$ in the centrality classes analysed of the Pb–Pb collisions at $\sqrt{s_{\text{NN}}} = 5.02$ TeV. For each analysed centrality class the average $\langle dN_{ch}/d\eta \rangle$ is reported.

The measured dN/dy are shown as a function of the $\langle dN_{ch}/d\eta \rangle$ in Figure 27, in red for the $\frac{3}{\Lambda}\text{H}$ and in blue for the $\frac{3}{\Lambda}\bar{\text{H}}$ where an increasing trend with the charged particle multiplicity is observed.

In many results, showed in the following, the yields are also corrected for the Branching Ratio (B.R.) of the 2 body decay channel, which is assumed to be 25% [1], and this corresponds to an increase by a factor 4 of all dN/dy .

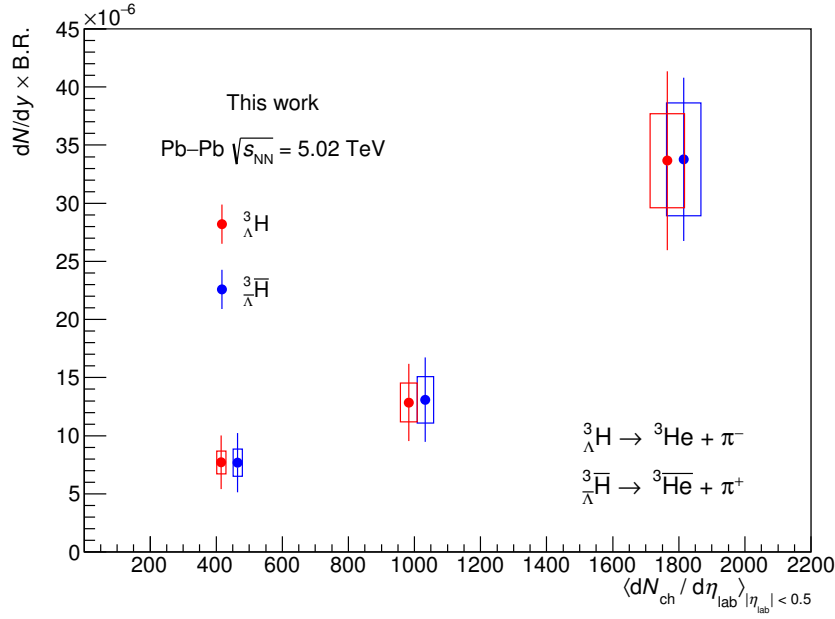


Fig. 27: dN/dy times the B.R. of the 2 body decay channel for the $\frac{3}{\Lambda}H$ (red) and the $\frac{3}{\Lambda}\bar{H}$ (blue). The vertical bar and the box are statistical and systematic uncertainty, respectively. Points relative to hypermatter and anti-hypermatter are horizontally shifted for visibility.

A more quantitative approach to investigate the scaling of the $\frac{3}{\Lambda}H$ production with the charged particle multiplicity is through the double ratio defined as:

$$\left(\frac{(\frac{3}{\Lambda}H + \frac{3}{\Lambda}\bar{H})_i}{(\frac{3}{\Lambda}H + \frac{3}{\Lambda}\bar{H})_j} \right) / \left(\frac{\langle dN_{ch}/d\eta \rangle_i}{\langle dN_{ch}/d\eta \rangle_j} \right) \quad (26)$$

where i and j are two different centrality classes in which the $(\frac{3}{\Lambda}\bar{H})\frac{3}{\Lambda}H$ dN/dy and the charged particle multiplicity $\langle dN_{ch}/d\eta \rangle$ are measured. This double ratio is evaluated for the 10–30%, 30–50% and 10–40% with respect to the results obtained in the most central class (0–10%).

Double ratios	
0–10%/10–30%	$1.44 \pm 0.34(\text{stat.}) \pm 0.19(\text{syst.})$
0–10%/30–50%	$1.03 \pm 0.28(\text{stat.}) \pm 0.14(\text{syst.})$
0–10%/10–40%	$1.27 \pm 0.24(\text{stat.}) \pm 0.16(\text{syst.})$

Table 24: Results of the double ratio as defined in Eq. 26 between the $\frac{3}{\Lambda}H + \frac{3}{\Lambda}\bar{H}$ dN/dy and the $\langle dN_{ch}/d\eta \rangle$ in the 0–10% centrality and the same values measured in the other three centrality classes. The dN/dy are divided for the B.R. of the 2 body decay channel which is assumed to be 25% [1].

The results of the double ratios are reported in Table 24, where the statistical and systematic uncertainties are propagated separately, and they are in agreement with the unity within 1σ , defined as the sum in quadrature of the statistical and systematic uncertainties. Especially in the first (0–10%/10–30%) and in the last (0–10%/10–40%), the uncertainties, dominated by the statistical component, are large (23–27%) and led to an agreement with the unity. Thus, the $(\frac{3}{\Lambda}\bar{H})\frac{3}{\Lambda}H$ production can be assumed to scale with the charged particle production, which means also with the number of participants and thus with the collision centrality.

The scaling with the charged particle multiplicity can be interpreted in the statistical hadronisation model as related to the volume of the medium created in the heavy ion collision. Indeed, according to Statistical

Hadronisation Models, the yield of each particle species depends on the volume V of the system and, since the size of V is assumed to increase while going from semi-central (30–50%) to central (0–10%) collisions, the average number of produced particles as well as the relative abundance of each of them are expected to increase.

Also in a coalescence approach [24] the dN/dy is expected to scale with the charged particle multiplicity, since an increased particle production lead to a higher number of baryons which could coalesce. However, other model implementations [25] describe the coalescence as an interplay between the $\langle dN_{ch}/d\eta \rangle$ and the increase of the volume of the system, measured through the Hanbury-Brown-Twiss radii of pions as described in [25], which lead to a reduction of the baryon density and thus to a less probability to coalesce while the centrality increases.

7.3 Antimatter-to-matter ratio

An important assumption for all the models describing the particles production at the LHC energies is that the baryon chemical potential μ_B is 0, the so called *transparency regime*, which has been also experimentally verified [26].

Both coalescence and thermal models predict that the antimatter-to-matter ratio is 1 for a system with vanishing baryon chemical potential. If the μ_B of the system is null or close to zero, the number of baryons and antibaryons in the system is the same and in the coalescence model there is no difference between the probability of producing a ${}^3_{\Lambda}\text{H}$ or an ${}^3_{\Lambda}\bar{\text{H}}$. In the thermal model approach the fugacity of a particle species $\lambda_i \propto e^{B_i\mu_B/T}$, where B_i is the baryon number of a particle species, is the only different term in the expected dN/dy of ${}^3_{\Lambda}\text{H}$ and ${}^3_{\Lambda}\bar{\text{H}}$. Thus, if a vanishing baryon chemical potential is assumed, the fugacities of ${}^3_{\Lambda}\text{H}$ and ${}^3_{\Lambda}\bar{\text{H}}$ coincide and their yields are the same according to the Statistical Hadronisation Model [27].

The ${}^3_{\Lambda}\bar{\text{H}}/{}^3_{\Lambda}\text{H}$ ratio has been estimated both as a function of the transverse momentum and as a function of the charged particle multiplicity. Figure 28 shows the ratio between the ${}^3_{\Lambda}\bar{\text{H}}$ and the ${}^3_{\Lambda}\text{H}$ p_T spectra measured in the 10–40% centrality class. The vertical bar corresponds to the statistical uncertainty and the box to the systematic one. The ratios are in agreement with the unity in the whole measured p_T region.

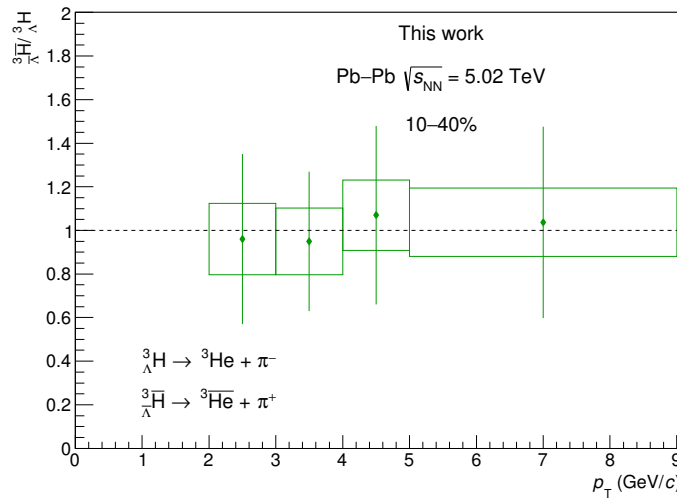


Fig. 28: ${}^3_{\Lambda}\bar{\text{H}}/{}^3_{\Lambda}\text{H}$ ratio as a function of p_T in the centrality class 10–40%. The dotted line represent the expected value of 1 under the assumption of $\mu_B=0$.

Figure 29 shows the same ratio as a function of the charged particle multiplicity, obtained in the three centrality classe 0–10%, 10–30% and 30–50%, which is also in agreement with unity.

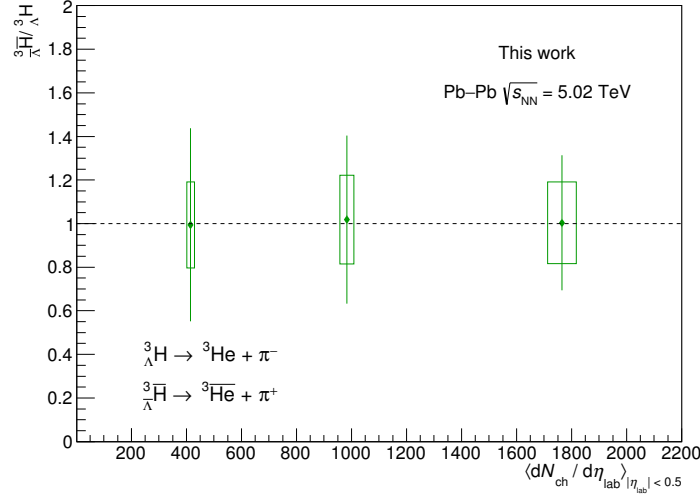


Fig. 29: $\frac{3}{\Lambda}\bar{H}/\frac{3}{\Lambda}H$ ratio as a function of the $\langle dN_{ch}/d\eta \rangle$ of the corresponding centrality class. The dotted line represent the expected value of 1 under the assumption of $\mu_B=0$.

783

Moreover, the numerical value of the ratios are reported in Table 26 for both cases. The agreement of these ratios with the unity confirm the assumption of μ_B close to zero for the model describing the particle and (hyper-)nuclei production at the LHC energies.

786

$\frac{3}{\Lambda}\bar{H}/\frac{3}{\Lambda}H$	
vs $\langle dN_{ch}/d\eta \rangle$	
0–10%	$1.01 \pm 0.27(\text{stat.}) \pm 0.19(\text{syst.})$
10–30%	$1.02 \pm 0.29(\text{stat.}) \pm 0.19(\text{syst.})$
30–50%	$0.99 \pm 0.35(\text{stat.}) \pm 0.18(\text{syst.})$
vs p_T (GeV/c)	
2–3	$1.01 \pm 0.49(\text{stat.}) \pm 0.17(\text{syst.})$
3–4	$0.97 \pm 0.32(\text{stat.}) \pm 0.16(\text{syst.})$
4–5	$1.05 \pm 0.48(\text{stat.}) \pm 0.16(\text{syst.})$
5–9	$1.03 \pm 0.50(\text{stat.}) \pm 0.15(\text{syst.})$

Table 25: Results of the $\frac{3}{\Lambda}\bar{H}/\frac{3}{\Lambda}H$ ratio as a function of the $\langle dN_{ch}/d\eta \rangle$ and of the p_T in the top and bottom part of the table. The ratio as a function of p_T is in the 10–40% centrality class.

7.4 $\frac{3}{\Lambda}H$ over ${}^3\text{He}$ ratio

787

In the heavy ion collisions, the evolution of the ratio between hypernuclei and nuclei dN/dy with the charged particle multiplicity is an important observables to investigate the hypernuclei production mechanism. In particular, the $(\frac{3}{\Lambda}\bar{H})\frac{3}{\Lambda}H$ over $({}^3\text{He}){}^3\text{He}$ ratio is evaluated as a function of the charged particle multiplicity $\langle dN_{ch}/d\eta \rangle$, using the relation:

791

$$\text{Ratio} = \frac{(dN/dy)_{\frac{3}{\Lambda}H}}{(dN/dy)_{{}^3\text{He}}} \quad (27)$$

According to the thermal model interpretation, at the LHC energies, the ratio is fixed by the temperature of the source, thus it is constant with the charged particle multiplicity evolution. For instance, the Statistical Hadronisation Model [27] predicts a ratio of 0.35 for $\frac{3}{\Lambda}H/{}^3\text{He}$ and 0.37 for $\frac{3}{\Lambda}\bar{H}/{}^3\bar{\text{He}}$.

792

793

794

The aforementioned ratio is evaluated for the 0–10% and 10–40% centrality classes, since the ${}^3\text{He}$ and ${}^3\overline{\text{He}}$ dN/dy have been measured in the same classes for the data sample of Pb–Pb collisions at $\sqrt{s_{\text{NN}}}=5.02$ TeV [6]. The ${}^3_\Lambda\text{H}$ and ${}^3_\Lambda\overline{\text{H}}$ dN/dy used in the calculation are corrected for the B.R. of the 2 body decay channel (B.R. = 25%).

Ratio			
	${}^3_\Lambda\text{H}/{}^3\text{He}$	${}^3_\Lambda\overline{\text{H}}/{}^3\text{He}$	$\langle dN_{ch}/d\eta \rangle$
0–10%	$0.49 \pm 0.10(\text{stat.}) \pm 0.12(\text{syst.})$	$0.56 \pm 0.11(\text{stat.}) \pm 0.16(\text{syst.})$	1756 ± 52
10–40%	$0.34 \pm 0.06(\text{stat.}) \pm 0.07(\text{syst.})$	$0.35 \pm 0.06(\text{stat.}) \pm 0.09(\text{syst.})$	826 ± 22

Table 26: Results of the $({}^3_\Lambda\overline{\text{H}}){}^3_\Lambda\text{H}$ over $({}^3\overline{\text{He}}){}^3\text{He}$ ratio in two different centrality classes in Pb–Pb collisions at $\sqrt{s_{\text{NN}}}=5.02$ TeV.

The results in the 0–10% centrality class are higher compared to the prediction, but still in agreement within 1σ , while the ratio in the 10–40% is closer to the expected one.

These results are also shown as a function of $\langle dN_{ch}/d\eta \rangle$ in Figures 30 and 31 as green circles for the ${}^3_\Lambda\text{H}$ and ${}^3_\Lambda\overline{\text{H}}$, respectively. The ratios are compared with those measured by STAR [13] (open square) in Au–Au collisions at $\sqrt{s_{\text{NN}}}=200$ GeV and ALICE [5] (red circle) in Pb–Pb collisions at $\sqrt{s_{\text{NN}}}=2.76$ TeV. In particular the values of the ratios measured in Pb–Pb collisions at two different energies, show a hint of increasing trend with the $\langle dN_{ch}/d\eta \rangle$, which is more pronounced for the ${}^3_\Lambda\overline{\text{H}}$. However, since the ${}^3_\Lambda\overline{\text{H}}$ yield is similar to that of the ${}^3_\Lambda\text{H}$ this slightly higher values of the ${}^3_\Lambda\overline{\text{H}}/{}^3\text{He}$ might be related to a lower ${}^3\overline{\text{He}}$ yield. Nevertheless, considering both the statistical and systematic uncertainties the ratios in the same class are in agreement.

In particular, the two ratios at the highest $\langle dN_{ch}/d\eta \rangle$ are in agreement with the GSI-Heidelberg [27] and THERMUS [28] statistical hadronisation model, which assume a thermal equilibrium for the medium created in the collision and a $T_{\text{chem}} = 156$ MeV, and with the Hagedorn resonance gas model [29]. On the other hand, the ratio measured in Pb–Pb collisions at $\sqrt{s_{\text{NN}}}=5.02$ TeV is slightly higher than the prediction of the non-equilibrium thermal model SHARE [30].

7.5 S_3 ratio

According to the authors of [31], the ${}^3_\Lambda\text{H}/{}^3\text{He}$ ratio can be dependent from the differences in the kinematics of different particle species due to collective motions. Thus they introduced the S_3 ratio defined as:

$$S_3 = \frac{{}^3_\Lambda\text{H}}{{}^3\text{He}} \times \frac{p}{\Lambda} \quad (28)$$

as a valuable tool to probe the nature of the medium created in the heavy ion collisions. In Eq. 28 Λ and p represent the measured dN/dy . This double ratio is extremely interesting since in thermal production it does not depend on the chemical potential of the particles and any additional canonical correction factor for strangeness is cancelled.

The ${}^3_\Lambda\text{H}/{}^3\text{He}$ ratio evaluated in the 0–10% and 10–40% centrality classes (see Sec. 7.4) is used to calculate the quantity reported in Eq. 28. Then also the Λ over p ratio is computed, using the preliminary yields [32, 19] obtained from the related production analysis in Pb–Pb collisions at $\sqrt{s_{\text{NN}}}=5.02$ TeV collected by the ALICE experiment. The results are reported in Table 27.

Moreover, the S_3 for the 0–10% class can be compared with other experimental results as well as with the theoretical predictions for the most central collisions in Figure 32. Only the GSI-Heidelberg and the Hybrid UrQMD models predict the S_3 for the most central collisions at the LHC energies and they are in agreement with the measurements presented in this work at 5.02 TeV. The GSI-Heidelberg is a thermal model [27] which predicts the particle yields assuming a complete thermalization of the medium, with

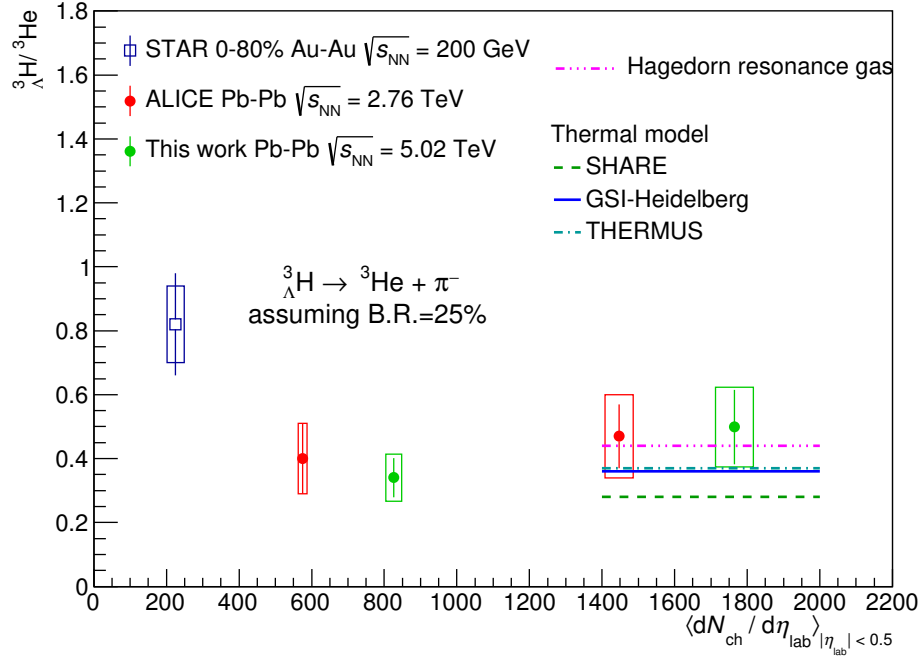


Fig. 30: $\frac{3\Lambda\text{H}}{3\text{He}}$ as a function of the average charged particle multiplicity $\langle dN_{\text{ch}}/d\eta \rangle$ measured in Pb–Pb collisions at $\sqrt{s_{\text{NN}}} = 5.02$ TeV (green circle). The results are compared with the published ratios of STAR (open square) [13] and ALICE (red circle) [5] and theoretical lines as described in the legend.

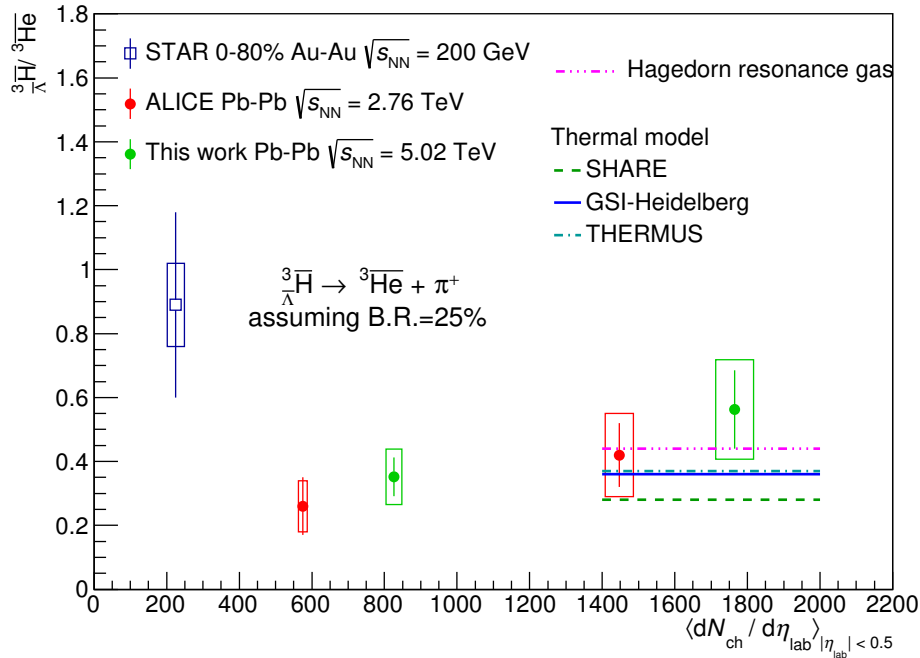


Fig. 31: $\frac{3\Lambda\text{H}}{3\text{He}}$ as a function of the average charged particle multiplicity $\langle dN_{\text{ch}}/d\eta \rangle$ measured in Pb–Pb collisions at $\sqrt{s_{\text{NN}}} = 5.02$ TeV (green circle). The results are compared with the published ratios of STAR (open square) [13] and ALICE (red circle) [5] and theoretical lines as described in the legend.

S_3		
	$\frac{{}^3\text{H}}{{}^3\text{He}} \times \frac{p}{\Lambda}$	$\frac{{}^3\bar{\text{H}}}{{}^3\bar{\text{He}}} \times \frac{p}{\Lambda}$
0–10%	$0.57 \pm 0.12(\text{stat.}) \pm 0.15(\text{syst.})$	$0.64 \pm 0.12(\text{stat.}) \pm 0.19(\text{syst.})$
10–40%	$0.40 \pm 0.07(\text{stat.}) \pm 0.09(\text{syst.})$	$0.24 \pm 0.04(\text{stat.}) \pm 0.07(\text{syst.})$

Table 27: Results of the S_3 ratio in two different centrality classes in Pb–Pb collisions at $\sqrt{s_{\text{NN}}} = 5.02$ TeV for the ${}^3\text{H}$ and ${}^3\bar{\text{H}}$. The $({}^3\text{H})_{{}^3\text{H}}$ dN/dy are corrected assuming a B.R. = 25% [1] for the 2 body decay channel.

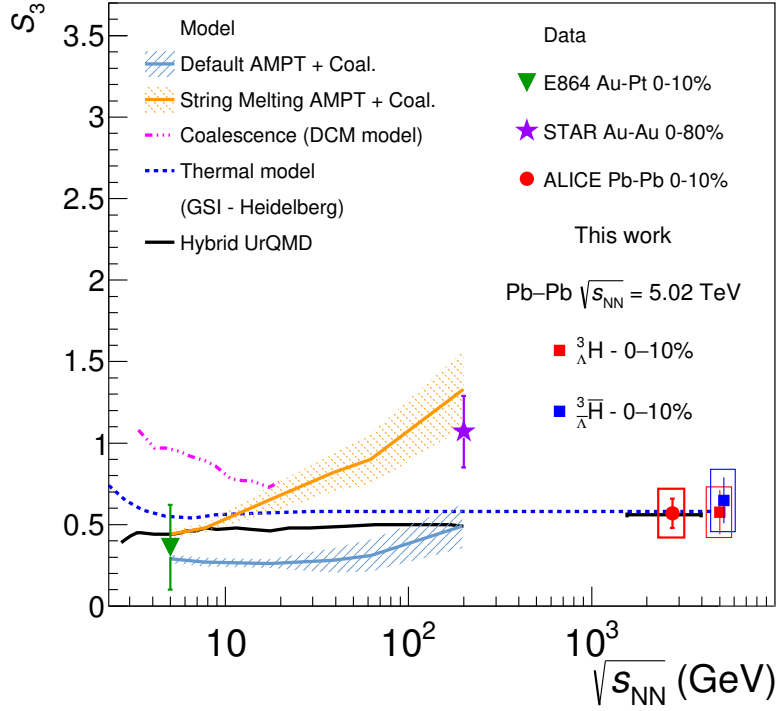


Fig. 32: Evolution of the S_3 with collision energy $\sqrt{s_{\text{NN}}}$. The red and blue full square are the results for the ${}^3\text{H}$ and ${}^3\bar{\text{H}}$ at 5.02 TeV, while the full markers are those obtained by other experiments and at different energies as explained in the legend. The blue square is horizontally shifted for visibility. The solid lines are the S_3 predictions by different thermal and coalescence models as described in the legend.

$\mu_B = 0$ and $T_{\text{chem}} = 156$ MeV. The Hybrid UrQMD model, instead, combines the hadronic transport approach with an hydrodynamical stage for the hot and dense medium created in the heavy ion collision. The evolution of S_3 is also predicted by the DCM (Dubna Cascade Model) [33] coalescence model and the AMPT (A Multi-Phase Transport Model for Relativistic Heavy Ion Collision) [34] coalescence model. They predict a rising trend with the collision energy which is not comparable with the results obtained by the ALICE experiment at 2.76 TeV [5] and in this note. The results are also in agreement with that measured by the E864 experiment at lower energy [31], while they do not confirm the rising trend shown by STAR [13].

7.6 Comparison with thermal model

The statistical hadronisation model predicts, as already described, the particles production using a thermodynamic approach, where the key parameter for the abundance of each particle species is the chemical freeze-out temperature T_{chem} .

However, in the case of the $(\bar{\Lambda}^3\text{H})_\Lambda$ production yield an important role is played also by the B.R. for the analysed decay channel. In this analysis the B.R. for the $\bar{\Lambda}^3\text{H}$ 2 body decay channel is assumed to be 25% [1], since it is also the same assumption done for the published results by STAR [13] and ALICE [5]. As a consequence, the theoretical predictions are also done as a function of the B.R. for the decay channel of the $\bar{\Lambda}^3\text{H}$.

Figure 33a and 33b show the measured $dN/dy \times \text{B.R.}$ as a horizontal line, where the bands represent statistical and systematic uncertainties added in quadrature, and the different theoretical models as lines. The theoretical predictions were performed assuming a possible variation of the B.R. in the range 15–35%, based on [35].

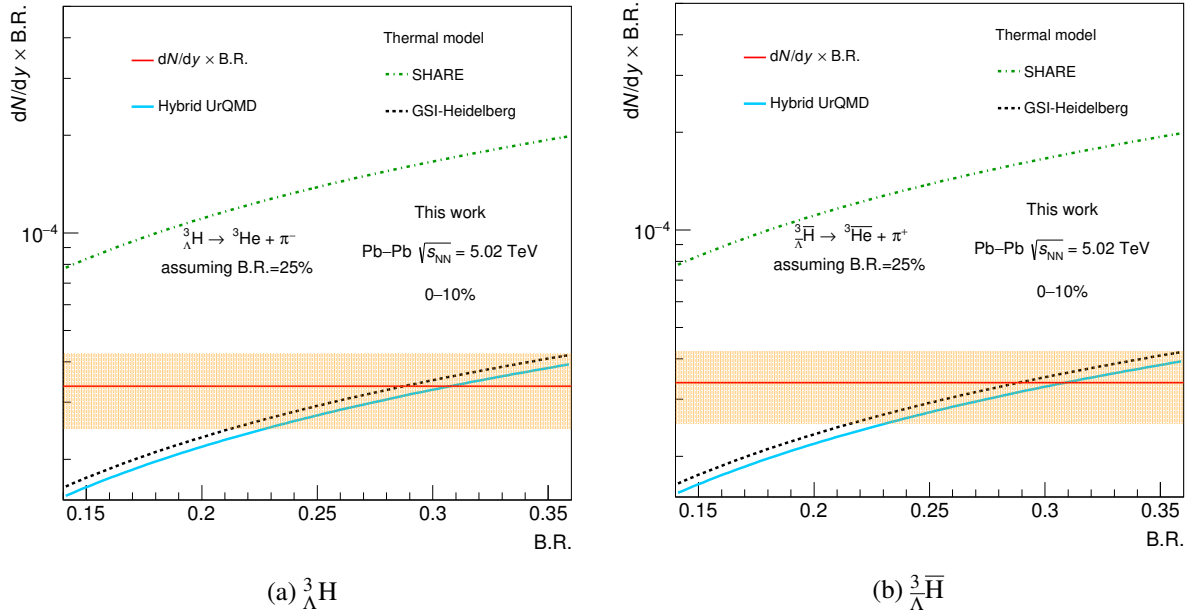


Fig. 33: $dN/dy \times \text{B.R.}$ as a function of the B.R. for the $\bar{\Lambda}^3\text{H}$ (a) and the $\bar{\Lambda}^3\text{H}$ (b). The red line is the measured yield where the B.R. is assumed to be 25% and the orange band is the sum in quadrature of the statistical and systematic uncertainties. The result is compared with three different theoretical model predictions as described in the legend.

The measured dN/dy for the $\bar{\Lambda}^3\text{H}$ and $\bar{\Lambda}^3\text{H}$ are in agreement with the statistical hadronisation model [27], which assumes a completely thermalized medium with a chemical freeze-out temperature of $T_{\text{chem}} = 156$ MeV, in the B.R. range 22–35%. Similarly, they agree with the Hybrid UrQMD model starting from B.R. $\sim 23\%$. The latter one is an hydrodynamical model, which combines the hadronic transport approach with an initial hydrodynamical stage for the hot and dense phase of a heavy ion collision. For the assumed B.R. of 25% both curves tend to underestimate the dN/dy . On the other hand, the non-equilibrium thermal model SHARE [30], which assumes a $T_{\text{chem}} = 138$ MeV and a non-thermalization of strangeness quark, overestimates the p_T -integrated yield by a factor which goes from 2 to 5 in the considered B.R. range.

7.7 Coalescence parameter

The class of the coalescence models for the production of $(\bar{\Lambda}^3\text{H})_\Lambda$ in heavy ion collisions can be investigated by computing the coalescence parameters B_3 for the $\bar{\Lambda}^3\text{H}$ and $\bar{\Lambda}^3\text{H}$, defined as:

$$B_3 = E_{\bar{\Lambda}^3\text{H}} \frac{d^3 N_{\bar{\Lambda}^3\text{H}}}{dp_{\bar{\Lambda}^3\text{H}}^3} \left(E_p \frac{d^3 N_p}{dp_p^3} \right)^{-2} \left(E_\Lambda \frac{d^3 N_\Lambda}{dp_\Lambda^3} \right)^{-1} \quad (29)$$

863 where the first term is the $(\frac{3}{\Lambda}\bar{H})_{\Lambda}^3H$ invariant momentum spectrum³, while the other two terms are the
 864 proton [19] and Λ [32] primary spectra, respectively. In this definition the neutron spectrum is assumed
 865 to be the same as the one of the proton, since the ALICE experiment can not measure it directly. Figure
 866 34a and 34b show the measured coalescence parameters B_3 as a function of the transverse momentum
 867 scaled by the mass number $A=3$ for the $\frac{3}{\Lambda}H$ (red marker) and the $\frac{3}{\Lambda}\bar{H}$ (blue marker) in Pb–Pb collisions
 868 at $\sqrt{s_{NN}}=5.02$ TeV and they show a similar trend. Moreover, the $\frac{3}{\Lambda}H$ is compared with the B_3 measured
 869 by the ALICE experiment in Pb–Pb collisions at $\sqrt{s_{NN}}=2.76$ TeV in the most central collision class
 870 (0–10%). Even if the comparison is done for the B_3 measured at two different energies, the plot shows
 871 an ordering with the collision centrality. This can be explained in the coalescence model framework as a
 872 decreasing volume V_{eff} of the source going from central to semi-central collisions. If the V_{eff} is bigger,
 873 the probability of having a proton, a neutron and a Λ close enough in the phase space to form a bound
 874 state is lower, thus the B_3 is smaller. On the other hand, the B_3 measured in this analysis for the $\frac{3}{\Lambda}H$
 875 and $\frac{3}{\Lambda}\bar{H}$ are obtained in narrow p_T intervals with respect to those measured in Pb–Pb collisions at $\sqrt{s_{NN}}=$
 876 2.76 TeV and show almost flat trend as a function of p_T/A , as assumed in the coalescence models.

³where $E \frac{d^3N}{dp^3} = \frac{1}{2\pi p_T} \frac{d^2N}{dp_T dy}$

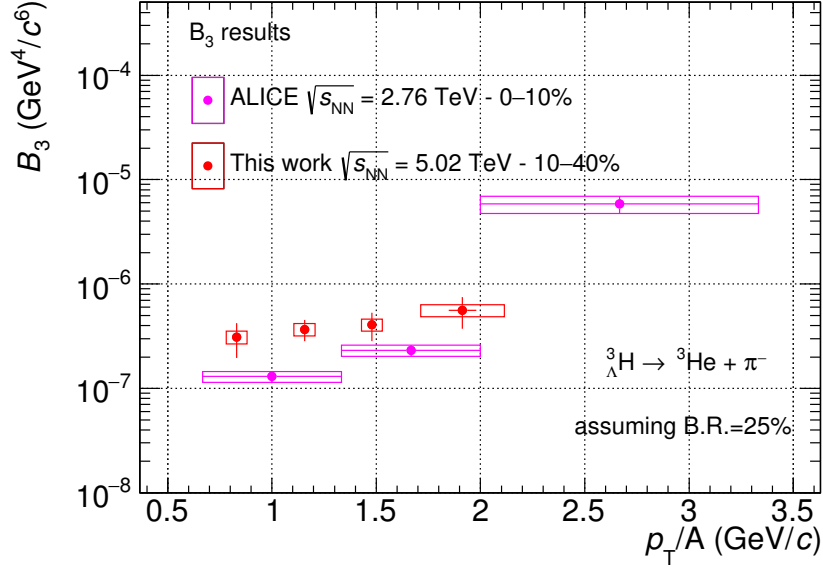
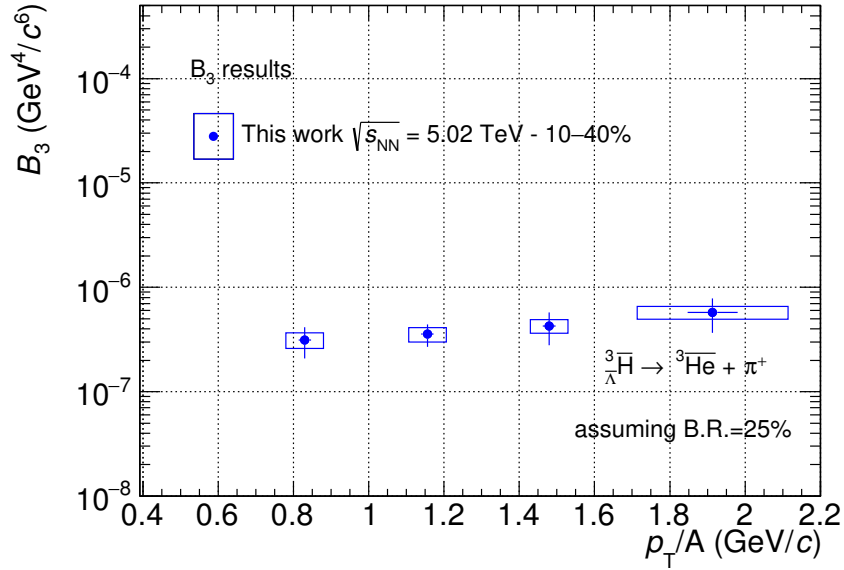

(a) ${}^3_{\Lambda}\text{H}$

(b) ${}^3_{\Lambda}\bar{\text{H}}$

Fig. 34: (a): ${}^3_{\Lambda}\text{H}$ B_3 as a function of p_{T}/A measured in the 10–40% centrality class of Pb–Pb collisions at $\sqrt{s_{\text{NN}}}=5.02$ TeV (red marker). The magenta points is the B_3 of the ${}^3_{\Lambda}\text{H}$ measured by the ALICE experiment in the 0–10% centrality class of Pb–Pb collisions at $\sqrt{s_{\text{NN}}}=2.76$ TeV [5]. (b): ${}^3_{\Lambda}\bar{\text{H}}$ B_3 as a function of p_{T}/A measured in the 10–40% centrality class of Pb–Pb collisions at $\sqrt{s_{\text{NN}}}=5.02$ TeV (blue marker).

7.8 Thermal fit

Finally, the ${}^3_{\Lambda}\text{H}$ and ${}^3_{\Lambda}\bar{\text{H}}$ dN/dy are included in the so-called “thermal fit”, which is a fit with a thermal model to the whole measured dN/dy at the same energy and in the same centrality class. In this case the fit is done using the hadrons, nuclei and hypernuclei yields measured in Pb–Pb collisions at $\sqrt{s_{\text{NN}}}=5.02$ TeV in the 0–10% centrality class. The fit is done with three different statistical thermal model: the GSI-Heidelberg [27], the THERMUS model [36] and the SHARE model [30]. They depends on the chemical freeze-out temperature T_{chem} , the baryon chemical potential μ_B and the source volume V . There are two additional parameters, called γ_q and γ_s , which allow the possibility to assume an incomplete thermal equilibration for the non-strange particles (i.e. π^\pm , p, d, ${}^3\text{He}$) and the strange particles (i.e. K_s^0 , Λ , Ξ , Ω , ${}^3_{\Lambda}\text{H}$), respectively. In all the models it is possible to fix or leave this γ factors free. However, the GSI-Heidelberg and the THERMUS model are always used fixing the γ_q to 1, assuming a complete thermalization of all non-strange particles.

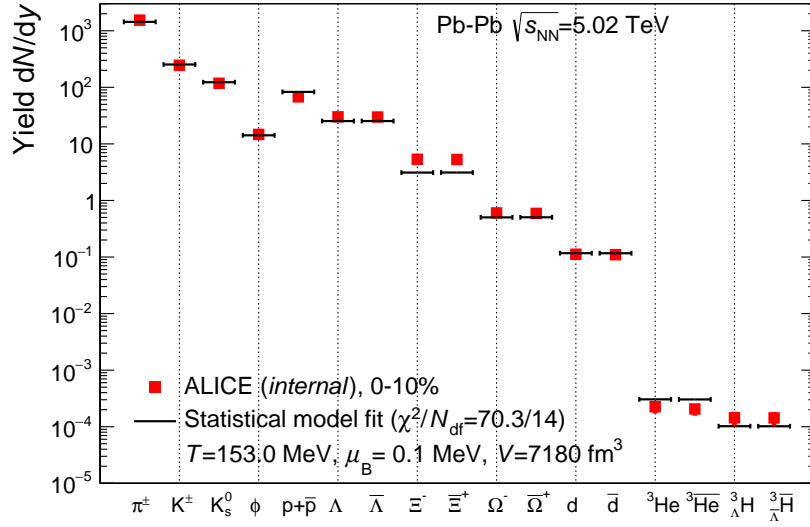
In every thermal fit the ${}^3_{\Lambda}\text{H}$ and the ${}^3_{\Lambda}\bar{\text{H}}$ dN/dy are corrected for the B.R. = 25% for the 2 body decay channel and then included in the list of the particle yields.

Figure 35a shows the results of thermal fit done with the GSI-Heidelberg model [37], while in Figure 35b the data are compared with the fit result through a ratio. The outcome of the fit is a chemical freeze-out temperature $T_{\text{chem}} = 153$ MeV and a baryon chemical potential $\mu_B = 0.1$ MeV, which is close to the expected null value. Particle yields of light flavor hadrons and (hyper-)nuclei are described over 7 order of magnitude with deviation within 3σ for most of them. Only the preliminary yields of protons and Ξ^\pm show a larger deviation. In particular, the deviation of the protons might be related to a baryon annihilation in the hadronic phase or to an incomplete hadron spectrum.

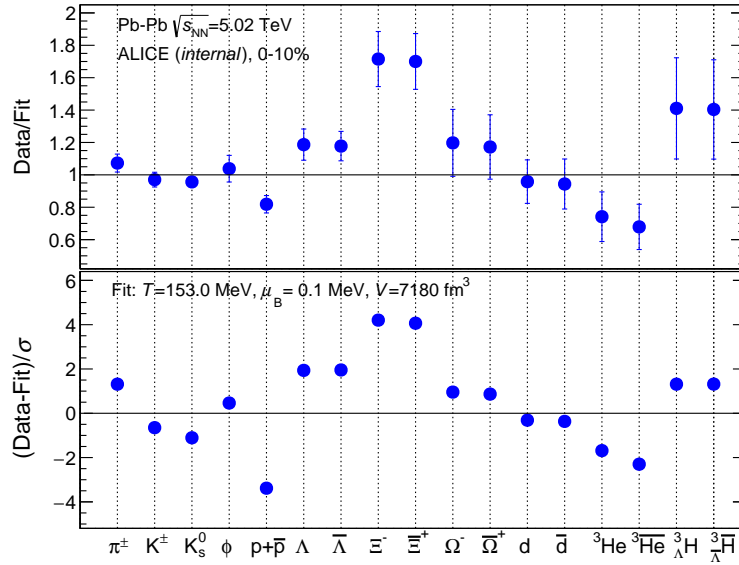
The fit with the THERMUS model [38] is shown Figure 36. In this case the K^* yield is not included in the fit and all the other dN/dy are fitted with two model configurations both with μ_B fixed to 0. In the first one the γ_s is not constraint, and this gave as result $\gamma_s = 1.17 \pm 0.04$ and $T_{\text{chem}} = 153 \pm 2$ MeV, which is in agreement with the T_{chem} of GSI-Heidelberg. The second configuration assumes $\gamma_s = 1$ and the result is still in agreement with the previous one but the temperature decreases to 152 ± 2 MeV since a complete strangeness equilibration is requested. Also the comparison of the volumes between the two configurations go in the same direction, since waiting for a complete thermalization of strange particle implies a larger time for the medium to thermalize and to expand.

The last thermal fit is done with the SHARE model [39] and is shown in Figure 37. The fit is performed with three different configurations of the model. The first one uses γ_s and γ_q as free parameters, which means assuming an incomplete equilibration of both non-strange and strange particles. Firstly, the fit is performed without including nuclei and $({}^3_{\Lambda}\bar{\text{H}}){}^3_{\Lambda}\text{H}$ leading to $T_{\text{chem}} = 160 \pm 10$ MeV, $\gamma_s = 0.95 \pm 0.22$ and $\gamma_q = 0.89 \pm 0.14$. Then it is done including the (hyper-)nuclear yield sector with strong reduction of the $T_{\text{chem}} = 139 \pm 1$ MeV and an increase of both $\gamma_s = 2.08 \pm 0.10$ and $\gamma_q = 1.63 \pm 0.05$. Also looking the results of the fit done with this configuration, shows a larger deviation of the nuclei and $({}^3_{\Lambda}\bar{\text{H}}){}^3_{\Lambda}\text{H}$ from the model. The second configuration of the SHARE model assumes a complete thermalization of the non-strange particle ($\gamma_q=1$) and the result is $T_{\text{chem}} = 154 \pm 3$ MeV, $\gamma_s = 1.14 \pm 0.05$, which are in agreement with the THERMUS model used in the same configuration. Finally, the fit is performed fixing both γ_s and γ_q , that is the other configuration used for THERMUS and the unique one for the GSI-Heidelberg and the result of $T_{\text{chem}} = 154 \pm 3$ MeV is in agreement with both two models.

The ${}^3_{\Lambda}\text{H}$ and the ${}^3_{\Lambda}\bar{\text{H}}$ dN/dy have been included in the thermal fits performed with three different thermal model, used in different configurations. The thermal models with a $T_{\text{chem}} = 153$ and γ_s unconstrained, better describe the dN/dy measured in this analysis and their deviation from the resulting fit is below 1σ . When the γ_s is fixed to 1 the yields are reproduced as well, but with a slightly higher significance. The closing remark from the thermal fits is that the ${}^3_{\Lambda}\text{H}$ and ${}^3_{\Lambda}\bar{\text{H}}$ can be produced thermally from the medium created in the heavy ion collision. This extremely surprisingly, since most of the theorists of the QGP



(a) Thermal fit to the dN/dy measured in Pb–Pb collisions at $\sqrt{s_{\text{NN}}}=5.02$ TeV with the GSI-Heidelberg model [37].



(b) Ratio of the measured dN/dy in Pb–Pb collisions at $\sqrt{s_{\text{NN}}}=5.02$ TeV with the result of the fit (top) and deviation from the fit result in number of σ (bottom).

924 tend to be in favor of a coalescence production mechanism for these loosely bound objects.

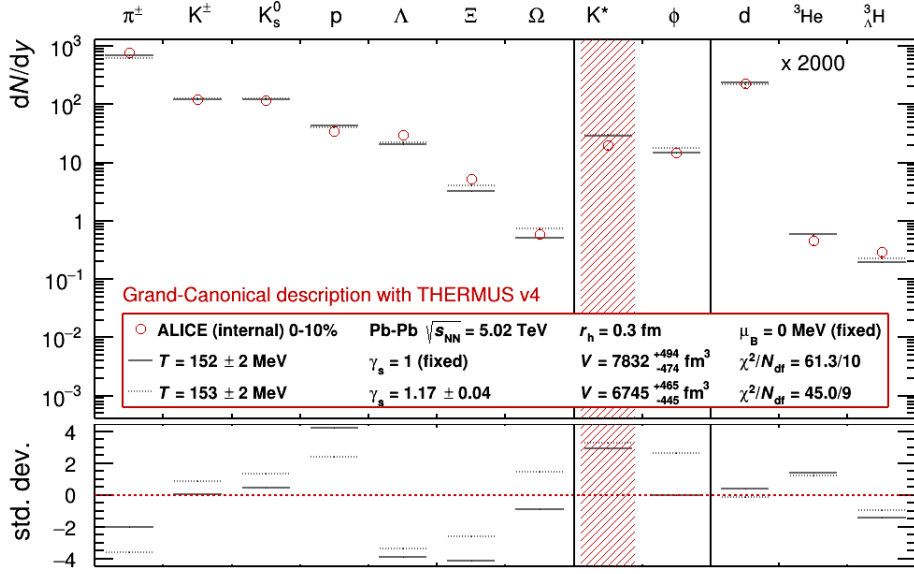


Fig. 36: Thermal fit to the dN/dy measured in Pb–Pb collisions at $\sqrt{s_{NN}} = 5.02$ TeV with the THERMUS model [38]. The bottom part show the deviation from the fit (Fit-data) in number of σ .

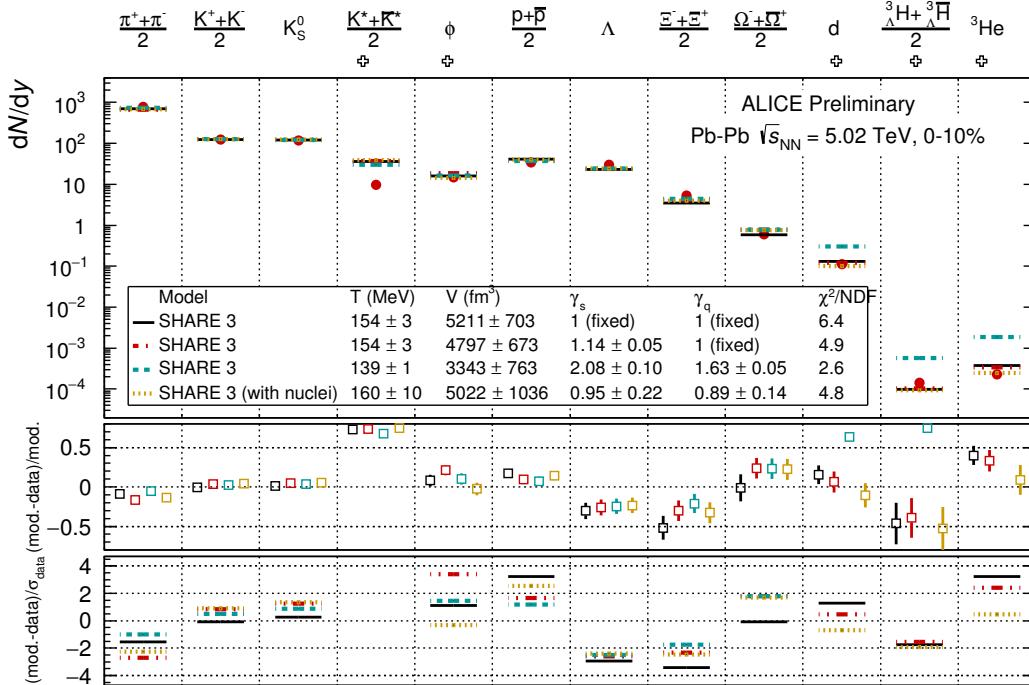


Fig. 37: Thermal fit to the dN/dy measured in Pb–Pb collisions at $\sqrt{s_{NN}} = 5.02$ TeV with the SHARE model [39]. The bottom part show the difference (Fit-data) normalized to the fit result and to the dN/dy uncertainty.

References

- [1] Kamada, H. *et al.*, Phys. Rev. C **57** (1998) 1595
- [2] Wang, X.-N. and Gyulassy, M., Phys. Rev. D **44** (1991) 3501
- [3] ALICE Collaboration, <https://aliceinfo.cern.ch/ArtSubmission/node/120>
- [4] <https://github.com/alisw/AlidPG/>
- [5] ALICE Collaboration, Phys. Lett. B **754** (2016) 360-372
- [6] ALICE Collaboration, <https://aliceinfo.cern.ch/Notes/node/626>
- [7] ALICE Collaboration, Phys. Rev. Lett. **116** (2016) 222302
- [8] ALICE Collaboration, ALICE-PUBLIC-2015-008 (2015), <https://cds.cern.ch/record/2118084>
- [9] ALICE Collaboration, *Int. J. Mod. Phys. A* **29** (2014) 1430044
- [10] Particle Data Group, Patrignani, C. *et al.*, Chin. Phys. C **40** (2017) 100001
- [11] ALICE Collaboration, Phys. Rev. C **93** (2016) 024917
- [12] D.H. Davis, *Nucl. Phys. A* **754** (2005) 3-13
- [13] STAR Collaboration, Science **328** (2010) 58
- [14] ALICE Collaboration, Eur. Phys. J C **73** (2013) 2496
- [15] ALICE Collaboration, Phys. Rev. Lett. **105** (2010) 072002
- [16] Evlanov, M.V. *et al.*, Nucl. Phys. A **632** (1998) 624
- [17] Kox, S. *et al.*, Phys. Lett. B **159** (1985) 15
- [18] R. Barlow, *Advanced Statistical Techniques in Particle Physics*, Proceedings, Conference, Durham, UK, March 18-22, 2002, pp. 134144, 2002
- [19] ALICE Collaboration, <https://aliceinfo.cern.ch/Notes/node/589>
- [20] ALICE Collaboration, <https://arxiv.org/abs/1802.09145> (2018) nucl-ex
- [21] Schnedermann, E. and Sollfrank, J. and Heinz, U.", Phys. Rev. C **48** (1993) 2462
- [22] ALICE Collaboration, Eur. Phys. J C **77** (2017) 658, 1707.07304
- [23] ALICE Collaboration, Phys. Rev. Lett **109** (2012) 252301
- [24] Chen, G. *et al.*, Phys. Rev. C **88** (2013) 034908
- [25] Scheibl, R. and Heinz, U., Phys. Rev. C **59** (1999) 1585 nucl-th/9809092
- [26] Floris, M. Nuc. Phys. A **931** (2014) 103 *Quark Matter 2014 - Proceedings*
- [27] Andronic, A. and Braun-Munzinger, P. and Stachel, J. and Stocker, H., Phys. Lett. B **697** (2011) 203 1010.2995
- [28] Cleymans, J. and Kabana, S. and Kraus, I. and Oeschler, H. and Redlich, K. and Sharma, N., Phys. Rev. C **84** (2011) 054916 1105.3719
- [29] Pal, S. and Greiner, W., Phys. Rev. C **87** (2013) 054905
- [30] Petran, M. and Letessier, J. and Petracek, V. and Rafelski, J., Phys. Rev. C **88** (2013) 034907 1303.2098
- [31] E864 Collaboration, Phys. Rev. C **70** (2004) 024902
- [32] ALICE Collaboration, <https://aliceinfo.cern.ch/Notes/node/588>
- [33] Steinheimer, J. *et al.*, Phys. Lett. B **714** (2012) 85 1203.2547
- [34] Lin, Z. *et al.*, Phys. Rev. C **72** (2005) 064901
- [35] Keyes, G. and Sacton, J. and Wickens, J.H. and Block, M.M., Nuc. Phys. B **67** (1973) 269
- [36] Wheaton, S. and Cleymans, J. and Hauer, M., Comp. Phys. Comm. **180** (2009) 84
- [37] Andronic, A. *private communication*
- [38] Hyppolite, B. *private communication*
- [39] Doenigus, B. *private communication*

⁹⁶⁹ [40] <https://alice.its.cern.ch/jira/browse/ALIROOT-7205>